AGU PUBLICATIONS

JGR

Journal of Geophysical Research: Solid Earth

RESEARCH ARTICLE
10.1002/2017JB015154

Key Points:
- The oceanic crust subducting below central Greece contains a 10 km thin, single-planed Wadati-Benioff Zone
- Transition between oceanic subduction (south) to continental subduction (north) is smooth rather than a tear
- Mantle wedge corner is relatively dry, but there is abundant silica enrichment above the forearc interface

Supporting Information:
- Supporting Information S1

Correspondence to:
F. Halpaap,
felix.halpaap@uib.no

Citation:
Halpaap, F., Rondenay, S., & Ottemöller, L. (2018). Seismicity, deformation, and metamorphism in the Western Hellenic Subduction Zone: New constraints from tomography. *Journal of Geophysical Research: Solid Earth*, *123*, 3000–3026. https://doi.org/10.1002/2017JB015154

Received 27 OCT 2017
Accepted 17 FEB 2018
Accepted article online 23 FEB 2018
Published online 20 APR 2018

Seismicity, Deformation, and Metamorphism in the Western Hellenic Subduction Zone: New Constraints From Tomography

Felix Halpaap[1], **Stéphane Rondenay**[1], **and Lars Ottemöller**[1]

[1]Department of Earth Science, University of Bergen, Bergen, Norway

Abstract The Western Hellenic Subduction Zone is characterized by a transition from oceanic to continental subduction. In the southern oceanic portion of the system, abundant seismicity reaches depths of 100 km to 190 km, while the northern continental portion rarely exhibits deep earthquakes. Our study investigates how this oceanic-continental transition affects fluid release and related seismicity along strike. We present results from local earthquake tomography and double-difference relocation in conjunction with published images based on scattered teleseismic waves. Our tomographic images recover both subducting oceanic and continental crusts as low-velocity layers on top of high-velocity mantle. Although the northern and southern trenches are offset along the Kephalonia Transform Fault, continental and oceanic subducting crusts appear to align at depth. This suggests a smooth transition between slab retreat in the south and slab convergence in the north. Relocated hypocenters outline a single-planed Wadati-Benioff Zone with significant along-strike variability in the south. Seismicity terminates abruptly north of the Kephalonia Transform Fault, likely reflecting the transition from oceanic to continental subducted crust. Near 90 km depth, the low-velocity signature of the subducting crust fades out and the Wadati-Benioff Zone thins and steepens, marking the outline of the basalt-eclogite transition. Subarc melting of the mantle is only observed in the southernmost sector of the oceanic subduction, below the volcanic part of the arc. Beneath the nonvolcanic part, the overriding crust appears to have undergone large-scale silica enrichment. This enrichment is observed as an anomalously low Vp/Vs ratio and requires massive transport of dehydration-derived fluids updip through the subducting crust.

1. Introduction

The Western Hellenic Subduction Zone (WHSZ) is home to large variations in subduction properties along strike, including subduction rate, trench retreat, occurrence of deep seismicity, and overriding plate extension. These variations are related, either directly or indirectly, to a change in convergence regime from the subduction of oceanic crust in the south to continental crust in the north. Of these variations, the rate of subduction is perhaps the most easy to explain — oceanic crust is less buoyant and therefore subducts at a faster rate than the more buoyant continental crust to the north. What causes the other subduction properties to vary, on the other hand, is less well understood. To gain better insight into the processes that affect subduction properties, we need to better characterize not only what is happening in the regions of oceanic and continental subduction but also the transition from one regime to the other.

While the southern portion of the WHSZ exhibits the classical features of a subduction zone, the northern portion proved more elusive until the last decade, when new seismic images clarified the situation. Indeed, with the northern portion not featuring any intermediate depth seismicity, there was no evidence that active subduction was taking place until high-resolution scattered wave images by Pearce et al. (2012) showed ongoing subduction of thick continental crust beneath northern Greece.

Given the presence of active subduction along the entire WHSZ, what happens at the transition from oceanic (south) to continental (north) subduction? Abundant surface observations yield a detailed picture of the top of the system. The subduction trench is discontinuous at the Kephalonia Transform Fault (KTF), with faster rollback of the oceanic slab causing a southwestward displacement of the trench in the southern segment. But the differential motion between the southern and northern segments is not concentrated at the KTF. Instead, it is distributed in an ≈100 km wide zone extending inland from the KTF into the Central Hellenic Shear

Zone (CHSZ) (see, e.g., Papanikolaou & Royden, 2007; Royden & Papanikolaou, 2011; Vassilakis et al., 2011). In this region, which includes the Gulf of Corinth, deformation occurs along generally E-W striking normal faults that crosscut older trench-parallel structures. How these patterns of deformation are translated from the surface to greater depth is, however, not yet resolved. Intermediate depth seismicity appears to terminate rather abruptly beneath the northeastern extension of the KTF (see, e.g., Hatzfeld & Martin, 1992), but it is unclear whether this termination is due to a simple change in composition of the subducted slab or to a change in the stress field associated with slab tearing, either along strike or beneath the KTF (e.g., Piromallo, 2003; Royden & Papanikolaou, 2011; Spakman et al., 1988). Seismic studies carried out until now have not been able to image directly the oceanic-to-continental transition, either due to limited resolution or insufficient data coverage.

Here we present a set of improved seismic velocity models and earthquake locations that give us new insight into processes that occur in the oceanic and continental subduction portions of the WHSZ, as well as in the transition between the two regimes. After a brief summary of the study area (section 2), we describe the methodologies (section 3) and the data set (section 4) used in our study. The analyses are performed on a new, integrated set of *P* and *S* wave arrival times from local earthquakes recorded at permanent and temporary stations deployed across Greece and neighboring countries. These are inverted with a modified version of the SIMULR16 package (Bleibinhaus, 2003) for local traveltime tomography and with hypoDD 2.1D (Waldhauser, 2012) for earthquake relocations. The results are presented (section 6) and interpreted (section 7) with the goal of better characterizing the transition between oceanic and continental subduction in western Greece and understanding how this transition affects seismicity, the stress field, and fluid processes across the region.

2. Geodynamic Setting

2.1. Structure of the Western Hellenic Subduction Zone

The Hellenic arc bends around the west and south of Greece, from the heel of Italy, around the Aegean toward southern Turkey along a 1,300 km long trench (see inset map in Figure 1). The large-scale setting is the collision between the African plate to the south, the Eurasian plate to the north, and the Arabian plate to the east. At the intersection sit the smaller Adriatic, Aegean, and Anatolian plates. Considering plate motions relative to the large Eurasian plate, the Aegean plate moves southwestward, overriding the Ionian lithosphere of the African plate to the south and the Adriatic microplate to the west (McKenzie, 1972). The Aegean plate also rotates counterclockwise together with the Anatolian plate due to the northward advance of the Arabian plate (Flerit et al., 2004; Reilinger et al., 2006). At the same time, the African plate moves northward at ≈2 mm/yr. The overall result is the Hellenic Subduction Zone.

The western portion of the system, which we have previously defined as the WHSZ, extends for 400 km along Greece's west coast (see Figure 1). It is in the middle of this subsegment that the transition from oceanic to continental subduction occurs. In the south, the oceanic crust of the Ionian sea consists of 6 km to 8 km of crystalline crust overlain by up to 6 km of sediments (Bohnhoff et al., 2001; Kokinou et al., 2005, 2006; Pearce et al., 2012). Measurements of magnetic remanence across the Ionian sea yield model ages of 220 Ma to 230 Ma (Speranza et al., 2012), making it one of the oldest preserved sea floors worldwide. In the north, the basement crust of the Adriatic plate has a thickness of 19 km to 30 km, with a progressive thinning toward the Corfu margin, and is covered by a 7 km thick carbonate platform (Finetti & Del Ben, 2005). This dichotomy results in a southern oceanic slab that is 3 to 4 times more negatively buoyant than the continental slab to the north and a current trench retreat of ≈35 mm/yr in the south compared to the 4 mm/yr to 10 mm/yr in the north (Royden & Papanikolaou, 2011; Vassilakis et al., 2011).

The differential rollback between the Ionian and Adriatic slabs is accommodated by the KTF, a dextral fault along which strong strike-slip earthquakes have occurred in the past (Karastathis et al., 2015; Sachpazi et al., 2000; Shaw & Jackson, 2010). At the KTF, the trench is offset horizontally by 140 km (Royden & Papanikolaou, 2011). However, the slab top on either sides of the fault appears to be vertically offset by less than 20 km in the 50–80 km depth range, suggesting an effective rollback of only 70 km in that part of the system (Pearce et al., 2012). While the trench is well defined south of the KTF, it is mostly covered by sediments and thus lacks a clear bathymetric signature to the north. Instead, the most prominent seafloor feature north of the KTF is the Apulian escarpment, which runs in a northwestern direction and represents the edge of the Adriatic (Apulian) microplate. As such, the Apulian escarpment represents the continuation, past the tip of the KTF, of the boundary between oceanic crust of the Ionian sea and the continental crust of the Adriatic plate

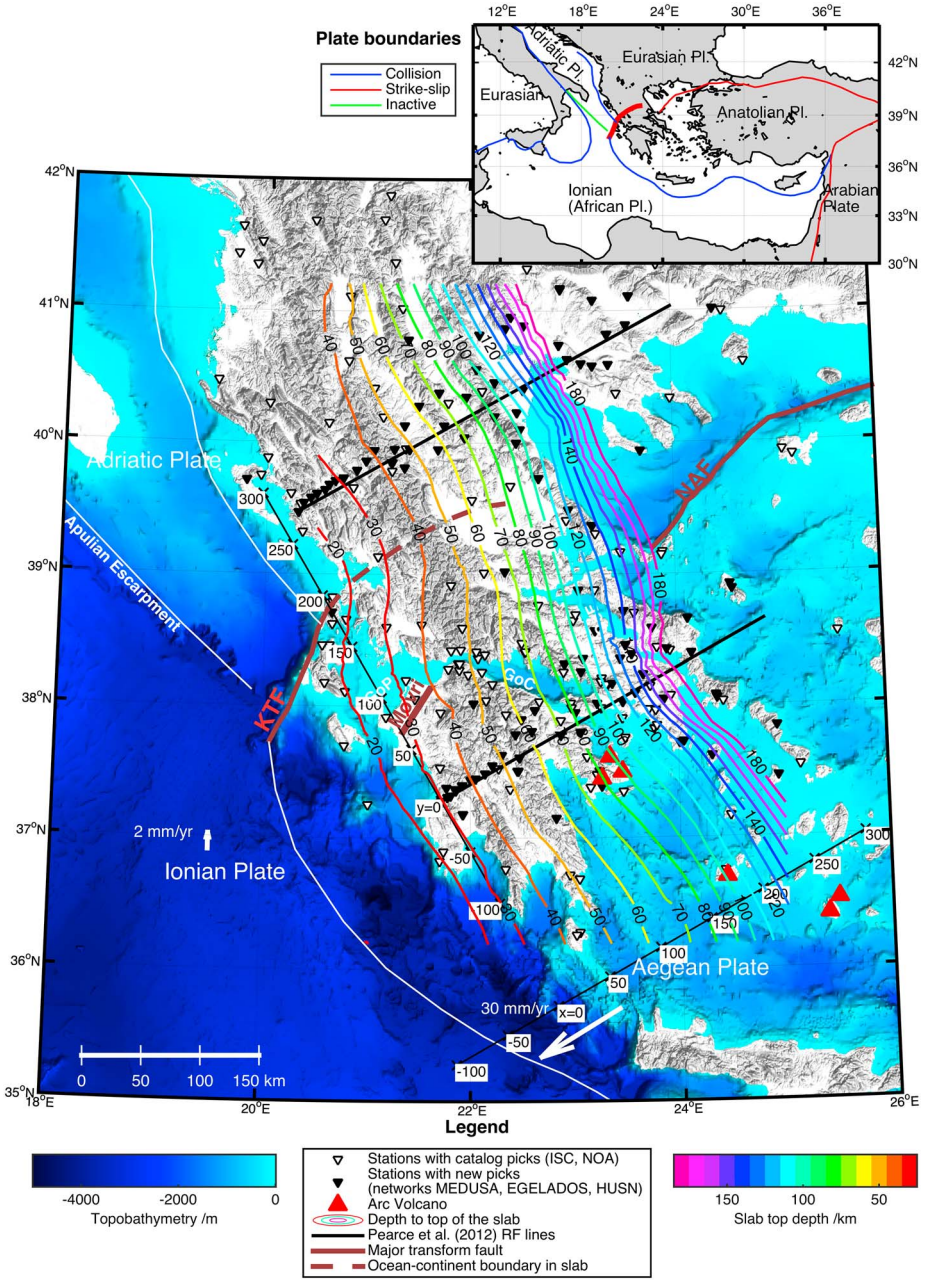

Figure 1. Map of mainland Greece and the Western Hellenic Subduction Zone, showing major geological features and the seismic stations used in this study. The inset shows an overview map of the eastern Mediterranean, with convergent plate boundaries in blue, transform boundaries in red, and inactive boundaries in green. The yellow rectangle in the inset marks the area shown in the main figure. Black numbers on white indicate the local coordinate system used for our analysis, whose origin is located at station XS.S001 and which is rotated by 30° counterclockwise from east (from a point at 39°N, 22°E), such that *x* increases in the direction of subduction dip and *y* increases along the strike of the subduction zone toward NW. See legend for the description of other symbols and lines.

(Finetti & Del Ben, 2005). But unlike the KTF, which is very active seismically, the Apulian escarpment is characterized as a passive margin without significant seismicity (Del Ben et al., 2015; Finetti & Del Ben, 2005).

Over the past 1–4 Myr, the KTF has connected to the North Anatolian Fault system through the so-called Central Hellenic Shear Zone (Papanikolaou & Royden, 2007; Royden & Papanikolaou, 2011). This has split the Aegean plate into a more active extensional backarc domain in the south than in the north. The Central Hellenic Shear Zone comprises a region of immature strike-slip faulting, spanning from the Corinth rift

to the Northern Gulf of Evia. It remains unclear whether shear deformation in the region is driven from the east by the Anatolian plate or from below by differential slab retreat. At the edge of the extensional domain, the Corinth rift is undergoing rapid extension at a rate of 10 mm/yr to 16 mm/yr, making it one of the youngest and fastest spreading rift basins on Earth (Nixon et al., 2016). The crust there is extensionally thinned, with thicknesses ranging from 25 km beneath the eastern Corinth rift to 45 km below the central Hellenides mountains (Zelt et al., 2005).

While the boundary between Adriatic and Ionian slabs has been fairly well constrained at the surface via direct observations, its structure at depth has been inferred mainly via geodynamic models until now. For example, models of Royden and Papanikolaou (2011) that are based on the age and thickness of accreted sediments suggest that Ionian lithosphere has been subducting since ≈8 Ma below the Peloponnesus, resulting in the subduction of 300 km of Ionian oceanic crust. This implies that the oceanic crust should have reached ≈150 km depth at 260 km horizontal distance from the current trench, assuming a shallow slab dip of 17° steepening to 45° below 90 km depth (based on Papazachos et al., 2000; Pearce et al., 2012; Zhu et al., 2015, and this study). The oceanic-continental plate boundary which subducts at the KTF should thus progressively bend toward the east, as indicated by the red dashed line in Figure 1, to join with the putative boundary of the subducted Ionian crust. At depth, the differential rollback between the two slabs could be accommodated by trench-normal tear, as has been suggested by Govers and Wortel (2005).

In addition to the structural differences described above, the transition from oceanic to continental subduction should also cause variations in the amount of fluid that enters the system. Indeed, there is seismic evidence that the Adriatic plate entering the WHSZ is drier than the Ionian plate (Finetti & Del Ben, 2005; Kokinou et al., 2005). This evidence is based on the detection of bending faults, which play an important role in hydrating the crust and mantle of a slab prior to subduction. For the WHSZ, such bending faults that penetrate the entire crust have been imaged in the Ionian (Kokinou et al., 2005) but not in the Adriatic (Finetti & Del Ben, 2005). This variation in hydration should have an influence on seismicity and magma generation along the WHSZ, something that we investigate in more details with our new models.

The current Hellenic volcanic arc starts just south of the Corinth rift, on the Methana peninsula, and extends for 500 km toward western Turkey. The arc includes the islands of Milos-Antimilos, Santorini, and Kos-Nisyros and is Pliocene to modern in age (Rizzo et al., 2016). It is not clear why there is no volcanic activity beyond Milos though, given that deep seismicity extends 150 km farther north along the strike of the WHSZ, suggesting that the slab dehydrates over that region. Based on a correlation between the distribution of volcanic rocks and the location of slab tears imaged by mantle tomography, Pe-Piper and Piper (2007) suggest that the current volcanism occurs due to advection of lithospheric mantle and melting associated with slab tearing.

2.2. Slab Images

Images of the Hellenic subduction zone at depth have been obtained through a range of seismic methods. These include seismic tomography at continental/mantle scales (e.g., Bijwaard et al., 1998; Koulakov et al., 2009; Piromallo, 2003; Spakman et al., 1988; Zhu et al., 2015) and local scales (Lamara, 2015; Papazachos & Nolet, 1997), receiver function studies (e.g., Gesret et al., 2011; Li et al., 2003; Sachpazi et al., 2016; Sodoudi et al., 2015), inversion of scattered teleseismic waves (e.g., Pearce et al., 2012; Suckale et al., 2009), active-source reflection imaging (e.g., Finetti & Del Ben, 2005; Kokinou et al., 2005, 2006; von Huene et al., 1997; Zelt et al., 2005), and refraction imaging (e.g., Bohnhoff et al., 2001). For a comprehensive overview of seismic studies that have been conducted until now in the region, we refer the reader to Suckale et al. (2009) and Pearce et al. (2012). Here we limit our review to those studies which are directly relevant to understanding the transition from oceanic to continental subduction in the WHSZ.

Tomographic studies have imaged the structure of the Hellenic subduction zone over a wide range of scales. At small scale, local earthquake tomography images the slab as a high-velocity tabular feature that dips gently from the surface down to 140 km depth (Lamara, 2015; Papazachos & Nolet, 1997). At larger scale, regional and teleseismic tomography shows an ≈150 km thick plate dipping at ≈45° between 200 km and 1,200 km depth (Bijwaard et al., 1998; Koulakov et al., 2009; Piromallo, 2003; Spakman et al., 1988; Zhu et al., 2015). While the lower portion of the slab appears fairly continuous across the mantle transition zone and into the lower mantle, the upper-mantle portion is discontinuous in most models beneath western Greece. Spakman et al. (1988) and Wortel and Spakman (2000) have suggested that this gap represents a trench-parallel slab tear which propagates from the north to the south.

Methods based on teleseismic receiver functions yield higher-resolution images than tomography in the 0–200 km depth range. Two profiles showing the subducted crust beneath southern and northern Greece were obtained by inversion of scattered teleseismic waves recorded at stations of the Multidisciplinary Experiment for Dynamic Understanding of Subduction under the Aegean (MEDUSA) (see black lines in Figure 1; Pearce et al., 2012; Suckale et al., 2009). In the south, the Ionian crust is seen by Pearce et al. (2012) as an 8 km thick low-velocity layer extending from 35 km depth beneath the coast to 90 km depth beneath Attica. In the north, the Adriatic crust is also seen as a low-velocity layer, but it is much thicker (20 km) and extends down to only 70 km depth (as imaged by *S* wave scattering potential $\delta\beta/\beta$). The termination of the low-velocity signature at depth has been interpreted by Suckale et al. (2009) and Pearce et al. (2012) as representing the transformation of crustal rocks into eclogite. Both the southern and northern segments dip at the same angle of 17° toward an azimuth of 60 ± 10°. Based on single-station receiver functions, Gesret et al. (2011) resolved similar dips in the 16° to 18° range but on average more easterly azimuths between 50° and 70°. More recently, a series of receiver function profiles by Sachpazi et al. (2016) revealed that the Ionian slab appears to be segmented into 30 km wide strips that run parallel to the subduction direction. These segments are delimited by vertical offsets of up to 10 km and are believed to be bounded by transform faults inherited from a spreading ridge. The profiles of Sachpazi et al. (2016) also showed a bend in the slab at 60 km depth, which is consistent with the geometry of the Wadati-Benioff Zone (WBZ) beneath the region (Hatzfeld, 1994; Papazachos et al., 2000).

Active source seismic studies yield the highest resolution across the WHSZ, though their depth range is usually limited to the crust and uppermost mantle. These approaches are particularly useful to characterize the slab before it reaches the trench. In the south, offshore surveys carried out in the Ionian sea (Kokinou et al., 2005, 2006) imaged thin oceanic crust entering the trench near the KTF. Near the Mediterranean ridge, another survey by von Huene et al. (1997) produced a 3-D image of what appears to be a mostly sediment-covered seamount. Based on these and other onshore-offshore profiles across Crete (Bohnhoff et al., 2001), the crust entering the trench in the southern part of the WHSZ appears to have an average thickness of 7 km and to be clearly oceanic in nature. In contrast, to the north, offshore profiles across the Adriatic sea have imaged a 19 km to 30 km thick crystalline crust (Del Ben et al., 2015; Finetti & Del Ben, 2005) moving toward the trench. Active source experiments have also been used to constrain the subducted slab at depth—for example, Zelt et al. (2005) identified reflected signals from the top of the slab at 70 km depth beneath the Gulf of Corinth.

2.3. Slab Seismicity

Shallow seismicity is abundant nearly everywhere in Greece, while intermediate depth earthquakes (deeper than 40 km) are confined to the slab. These intermediate depth earthquakes account for ≈30% of earthquakes above magnitude 5 compiled by the International Seismological Centre (2017) since 1960 for the region. In western Greece, large earthquakes of magnitude $M \geq 6$ occur both in the overriding and subducting plates (Durand et al., 2014). Two regions of the overriding plate that are particularly active seismically are the Corinth rift and the KTF. Large earthquakes related to the subducting plate occur both at the subduction interface and at intermediate depth within the slab. Focal mechanisms of regional events are routinely calculated by the National Observatory of Athens (NOA) (Konstantinou et al., 2010) for earthquakes down to magnitude $M_W = 4$. There are also more focused compilations of reviewed focal mechanisms by Shaw and Jackson (2010) and Serpetsidaki et al. (2016). In general, subduction-related earthquakes are thought to result from two main causes in the WHSZ.

1. The slab breaking up, plunging downward, rolling back, and slipping along the interface with the overriding plate (Durand et al., 2014; Papazachos et al., 2000). This sequence of earthquakes includes normal faulting in the slab and thrust faulting along the interface, with both types of faulting occurring in the direction of subduction.
2. Compression parallel to the trench due to the convex shape of the slab, which results in arc-parallel thrusting (Benetatos et al., 2004; Rontogianni et al., 2011).

Earthquake relocation studies have been carried out using increasingly widespread and dense seismic networks. An early investigation by Papazachos et al. (2000) showed a steepening of the WBZ at 70 km depth below the Peloponnesus (Papazachos et al., 2000). Based on the newer earthquake catalogs, (Sachpazi et al., 2016) suggested that intermediate depth earthquakes cluster along slab-parallel lines, possibly denoting inherited transform faults. While these two studies relied on 1-D background velocity models, others used more general treatments based on nonlinear inversion (e.g., Brüstle, 2012) and/or double difference

(e.g., Galanis et al., 2006; Karakonstantis & Papadimitriou, 2010). Still, none of these studies has yet tackled the high degree of uncertainty related to deep earthquake locations in the WHSZ and their relation to structures imaged by receiver functions.

3. Methods

In this study, we seek to improve earthquake locations and obtain 3-D models of *P* wave velocity and Vp/Vs ratio for the WHSZ. To do so, we adopt a strategy that comprises three stages: (1) 1-D inversion of *P* and *S* wave arrival times, to build a starting model for the tomography; (2) local earthquake tomography, in which we invert *P* and (*S*-*P*) wave arrival times to obtain 3-D velocity models of the subsurface; and (3) double-difference relocation, to increase the accuracy of relative earthquake locations. Even though there exists a scheme that combines stages 2 and 3 (tomoDD; Zhang et al., 2004), we opted for a stepwise approach. This gives us access to improved forward solvers for the tomography and relocation. For the tomography, we use SIMULR16 (Bleibinhaus, 2003), an upgrade of the popular SIMULPS package (Eberhart-Phillips, 1990; Thurber, 1983; Thurber & Eberhart-Phillips, 1999). While the ray tracer of SIMULPS was shown to be accurate for arrays smaller than 50 km × 50 km (Evans et al., 1999), that of SIMULR16 can handle larger arrays such as ours, which is 500 km × 500 km. To obtain relative earthquake locations, we use version 2.1D of the hypoDD double-difference software package (Waldhauser, 2012). The advantage of this version is that it can handle a 3-D background velocity model, in contrast to previous versions which used a 1-D model. This allows us to use directly our resulting 3-D tomographic model to relocate the earthquakes. Below, we describe the three stages of our analysis in more details.

3.1. One-Dimensional Velocity Inversion

In the first stage, we invert our arrival time observations to generate an optimal 1-D velocity model which we then use as a starting model for the 3-D inversion. This is a key step as it has been shown that the results of 3-D traveltime inversion are highly dependent on its starting model, and thus, great care should be placed into determining this model (see, e.g., Kissling et al., 1994). Here we use the program VELEST (Kissling et al., 1994), which inverts *P* and *S* arrival times for 1-D velocity structure and hypocenter coordinates using a damped least squares iterative inversion scheme. VELEST also requires a starting model and an initial parameterization (i.e., number of layers and layer thicknesses), which we set by combining information from various sources in the literature. The crustal part is based on the 1-D model of Haslinger et al. (1999), which was obtained by local earthquake tomography in the Gulf of Arta. Below the base of that model (45 km), we use velocities from the global AK135 model (Kennett et al., 1995). As for the parameterization, we introduce thin layers close to the expected average Moho depth from previous receiver function studies (Sachpazi et al., 2016), so that VELEST can return a sharp velocity increase in that prescribed depth rage. The introduction of low-velocity layers in the initial model is prohibited by VELEST, as such structure would produce 1-D solutions that are more complicated than necessary.

3.2. Local Earthquake Tomography

In the second stage, we use SIMULR16 to iteratively relocate earthquakes and invert for the 3-D Vp and Vp/Vs ratio structure. SIMULR16 employs a linearized damped least squares inversion scheme for perturbing an initial velocity model. A damping parameter is used to control the maximum perturbations per iteration, which is usually determined from an *L* curve test to find the best trade-off between root mean square (RMS) residual and data variance. The inversion is linearized through Fermat's principle, which states that the ray's traveltime is stationary for small changes in the raypath (Bleibinhaus, 2003). And since only small changes of raypath are allowed at each step, the data kernel *G* can also be assumed to remain constant within one iteration. Each iteration updates the model parameters by a perturbation Δm, which includes changes in Vp and Vp/Vs ratio from the previous iteration models as well as station corrections. This perturbation can be expressed as follows:

$$\Delta m = \left(G^T G + \Theta^2 E\right)^{-1} \times \left(G^T \Delta d\right), \tag{1}$$

where *G* is the data kernel, Θ is the damping parameter, *E* is the error matrix, and Δd is the residual between the current model's synthetic traveltimes and the traveltime observations *d*. Hypocenters are relocated after each update of the velocity model by individual least squares inversions for each earthquake. In both layers of inversion, the iterative process is stopped either when a maximum number of iterations is reached (15 for velocity models and 10 for hypocenters) or when an *F* test indicates that no significant improvement in data residuals has occurred from one iteration to the next.

At each update of the velocity model, raypaths are calculated through a process that combines an artificial ray tracer (ART) and a pseudo bending ray tracer (PB) (as described in Um & Thurber, 1987). Our version of SIMULR16 comprises two improvements that permit the accurate treatment of long raypaths (i.e., greater than 80 km), which have been shown to introduce significant errors in the solution when using the traditional ART-PB approach (Haslinger & Kissling, 2001). First, it includes the modified ray tracer of Bleibinhaus (2003), which improves the ART and includes an iterative segmentation during PB to compute the rays more accurately in very heterogeneous areas. These changes increase computational cost, and they also improve ART-PB's accuracy by more than 1 order of magnitude for distances above 140 km (Bleibinhaus, 2003), which benefits this study since many of our raypaths exceed this distance. Second, we implement a new correction to account for the sphericity of the Earth which, if ignored, can yield traveltime errors of up to 1–2 s for raypaths exceeding 500 km. We chose the "sphere-in-a-box" approach from Theunissen et al. (2018). This approach calculates hypocenters and raypaths in a Cartesian coordinate system where the topography, station locations, and initial hypocenters are converted from latitude, longitude, and depth to the local left-handed Cartesian coordinates x (azimuth 60°), y (azimuth 330°), and z (down) (Theunissen et al., 2018). This way, we can represent the subduction zone and related seismicity in their true geometry. It also lets us build an initial 1-D velocity model that honors the geospherical shape, with an additional adjustment of surface elevations based on the ETOPO1 topography model (Amante & Eakins, 2009).

In terms of parameterization, we use a variable grid spacing and a regridding strategy that help improve the robustness of the final models. The SIMUL family of programs operates on a rectangular grid with variable node spacing where inversion nodes can be turned on or off—with values at off nodes being interpolated (Thurber & Eberhart-Phillips, 1999). This allows to vary the number of nodes as a function of ray coverage (supporting information Figure S1), Fresnel zone size, and expected structure. For example, in our application, we use a smaller node spacing in the crust to better implement the geospherical correction and improve the recovery of the Moho. Nodes are automatically turned off when their derivative weight sum—a measure of ray hits and residual—falls below a certain threshold (usually 10). This helps increase the determination ratio (number of observations versus number of unknowns) and thus the robustness of the inversion. The overall grid spacing is decreased over the course of the inversion to build robust starting models for progressively detailed inversions. A first set of inversions is performed on a coarse grid (12 × 13 × 18 nodes), followed by two additional sets with more refined grids (23 × 23 × 21 and 27 × 27 × 24 nodes; see Figure S1). The final model of each set of inversions serves as the starting model for the next set.

Throughout the various inversion steps, the observations are weighted based on picking errors, event-station offsets, and traveltime residuals. Picking errors are set at a constant value of 0.2 s for all observations (see section 4 for further discussion). In terms of event-station offsets, observations made at offsets ≤100 km receive a weight of 100%; those that are between 100 km and 400 km see a linear weight reduction between 100 and 50%, and those in the 400 km to 900 km range receive between 50 and 25%. Offsets above 900 km are not considered. As for traveltime residuals, full weight is applied to observations that yield residuals <0.6 s. Then the weights are reduced linearly from 100% to 2% for residuals between 0.6 s and 3.0 s and from 2% to 0% for residuals between 3.0 s and 7.0 s. No inversion data are discarded with this weighting strategy, since our preprocessing already gets rid of arrival time picks that yield more than 5 s residuals after initial relocation with a 1-D model.

3.3. Double-Difference Relocation

In the third stage, we improve relative locations of earthquake hypocenters computed in stage 2 by applying the double-difference method of Waldhauser and Ellsworth (2000). Double-difference relocation considers traveltime differences between pairs of nearby earthquakes. Owing to the earthquakes' proximity, one can assume that the raypaths connecting them to a given station are nearly identical except for the short segment separating them and that the velocity is constant over that segment. Given these assumptions, the difference in traveltime between the two events at a given station is only a function of their separation in space, and a precise measure of this separation can be obtained via a quantity called the "double difference," which is expressed as follows (see Waldhauser & Ellsworth, 2000):

$$dr_k^{ij} = \left(t_k^i - t_k^j\right)^{\text{obs}} - \left(t_k^i - t_k^j\right)^{\text{cal}}, \tag{2}$$

where dr_k^{ij} is the double difference at station k for events i and j and t_k^i and t_k^j are the traveltimes of the two events at that station, which are either observed ("obs") or calculated by ray tracing through a background

velocity model ("calc"). Here we use hypoDD version 2.1D (Waldhauser, 2012) to calculate the raypaths and traveltimes through our resulting 3-D model from stage 2. This yields more accurate traveltime values than the original version of hypoDD, which relies on 1-D background models that cannot address the high level of heterogeneities found in subduction zones. With double differences from multiple stations and events, one then forms a system of equations that can be solved for hypocentral parameters (i.e., perturbations Δx, Δy, Δz, Δt to the initial hypocentral locations that minimize the various double differences). This system of equations can be solved either with a singular value decomposition algorithm for <700 events (threshold for this survey due to 32 bit memory restrictions), which allows accurate error estimation, or with the conjugate gradient algorithm for a larger number of events.

4. Data

The data set used in this study consists of *P* and *S* wave arrival times for earthquakes that occurred beneath the study area. It comprises a combination of our own manual picks from recordings made at temporary/permanent stations and arrivals from reviewed events located by the International Seismological Centre (ISC) and the NOA. We consider only earthquakes that initial estimates place within our inversion domain—a region encompassing all of mainland Greece and the Peloponnesus (Figure S1). We thus start with an initial set of 3,063 earthquakes (see left panels in Figure S2 in supporting information) and follow a quality-control workflow to extract events/data that will ensure robust inversion results. In this section, we describe how we pick/integrate the arrival time data and how we select the high-quality data that we retain for further analysis.

We manually pick arrival times from ISC-listed events recorded between 2006 and 2009 by the MEDUSA network and by available EGELADOS and NOA stations. We pick all deep events with magnitudes $M \geq 3$, but due to the abundance of shallow events, we limit our inversion data set to shallow earthquakes with magnitudes greater than 4. All clearly visible *P* and *S* arrivals are picked in SEISAN (Havskov & Ottemöller, 1999), and a four-level quality rating is applied: (1) *clear impulsive*, (2) *clear emergent*, (3) *unclear emergent*, characterized by significant variations in apparent arrival depending on filter frequencies, and (4) *questionable arrival*, characterized by high noise levels, especially for *S* arrivals. We use these quality ratings to weight our picks in the subsequent relocation and tomographic inversion, that is, by 100%, 50%, 25%, and 12.5%, respectively. If possible, we pick these arrivals without filtering the seismograms, but weaker events often require a filter with corner frequencies between 2 and 15 Hz.

Our data set is supplemented with ISC- and NOA-published arrival times from other stations in Greece and Albania. These new data are selected by applying the following rules: (1) if picked by several agencies, the arrival times of one event at a given station must not differ by more than 1 s; (2) for two arrival times published within that range, we choose the earlier arrival; (3) for three or more arrival times we choose the median value. For a few publicly available permanent stations, we are able to compare our picks to the picks that other agencies sent to the ISC. Comparing absolute differences, we find that these *P* picks ($n = 1,041$) deviate on average by 0.45 s from our picks. Though this deviation may seem large, it is biased by picks associated with noisy events recorded at large offsets. And since these long-offset picks are automatically downweighted by the inversion (see section 3.2), the effective deviation on meaningful picks is in reality a lot smaller.

The robustness of the assembled arrival time picks is assessed through an initial set of hypocenter relocations computed in SEISAN with a standard 1-D background velocity model. At this stage, we use three criteria to further refine the events that will be used for tomographic inversion: (1) azimuthal ray coverage, (2) number of observations, and (3) size and shape of the error ellipse. We do not apply hard limits on each of these selection criteria, as this would restrict our data set to earthquakes located directly below densely instrumented areas. Instead, a more flexible selection helps us retain earthquakes located near the boundaries of the inversion domain, particularly those offshore toward the trench. These events may yield slightly larger hypocentral errors due to one-sided coverage, but they can considerably improve ray coverage in the deeper regions of the tomographic model (Koulakov et al., 2009). In general, we try to avoid earthquakes that yield gaps in azimuthal ray coverage greater than 180° but keep those for which all arrival time residuals were small (< 3 s) and the hypocentral depth estimate appears robust (i.e., resolved with a clear global residual minimum at this depth). This leads to a set of earthquakes with azimuthal coverage gaps that average 102.5°, in which only ≈13% have gaps larger 180°. All retained earthquakes are observed by at least eight stations, with an average of ≈28 stations per earthquake. Hypocentral errors are restricted to under 15 km and 20 km in the horizontal and vertical directions, respectively, and preferably below 10 km in both directions for earthquakes

that have comprehensive azimuthal coverage. After the event selection has been refined based on the three criteria, we reject arrival time picks that consistently yield data residuals > 5 s after several (usually 8) rounds of relocations and further data winnowing.

The resulting data set contains a total 42,512 picks (29,333 *P* and 13,179 *S* picks) of which 8,646 were picked and weighted in this study. These stem from 1,070 events, which include 104 deep events published by the ISC over the 1990–2006 period, 730 deep events published by NOA since 2008, and 235 ISC-published events observed by the MEDUSA network. Given the multiple sources of data, it is difficult to determine a consistent picking error that is useable to assess hypocenter errors in the subsequent analyses. Errors for our manual picks are on average <0.1 s and 0.2 s for *P* and *S* waves, respectively (i.e., based on Diehl et al., 2002). Thus, we choose the more conservative value of 0.2 s for all our picks to take into account the inclusion of ISC and NOA data. This value is deemed conservative because it is at the upper range of picking errors used in other comparable studies using similar inversion codes (0.03 s to 0.2 s; Eberhart-Phillips & Bannister, 2010; Reyners et al., 2006). Though it is smaller than the average difference of 0.45 s observed between some of our picks and ISC/NOA picks, the downweighting of long-offset observations should reduce this difference to below 0.2 s. Nevertheless, to ensure that we do not misrepresent our uncertainties, we later discuss how doubling this picking error affects hypocenter errors.

5. Resolution

In this study, resolution pertains to both the resulting velocity models and hypocenter locations. For the velocity models, we assess the resolution by conducting checkerboard tests and comparing the inversion results of two independent data subsets. Here we only discuss the checkerboard tests. The inversion results of independent data subsets (one based on our new picks and one based on data published by NOA since 2008) and their comparison to the final model are described in the supporting information (see Figures S4 and S5). This test demonstrates that the recovery of robust velocity features is independent of station setup, hypocenter distribution, and picking source. With regard to hypocenter locations, we measure how errors decrease progressively through the iterative relocation processes described in stages 1–3 of the section 3.

5.1. Checkerboard Tests

With the checkerboard tests, we assess how well an anomaly can be recovered as a function of its size, sharpness, and location within the inversion domain. Since this is the most commonly used resolution test in local earthquake tomography, the community has established standard guidelines. We follow those of Koulakov et al. (2009) whenever they are compatible with SIMULR16's input and output structure. We start by creating a series of models based on our final tomographic model, in which velocities are alternately perturbed by ±5% on grids of progressively decreasing mesh size, from 120 km × 120 km × 120 km to 30 km × 30 km × 30 km. We then calculate synthetic traveltimes from this perturbed velocity model. To these synthetic traveltimes, we add Gaussian-distributed random noise with a standard deviation of 0.2 s, our estimated picking error. Lastly, we invert for velocity structure and hypocenter locations using our final tomographic model without checkerboard perturbations as starting model.

The outcome of our resolution test is shown in Figure 2, where we display inversion results for the smallest grid sizes which recovers the checkerboard structure adequately, that is, 45 km × 45 km × 45 km for *P* velocities and 60 × 60 × 60 km for Vp/Vs ratio. These represent good estimates of the smallest structure we can expect to image robustly beneath western Greece. As shown in the depth slices of Figure 2, the well-resolved volume thins out with depth in regions where earthquake sources become confined to a narrow band. However, the amplitude of the velocity contrasts is recovered accurately down to depths of 80 km.

5.2. Hypocenter Error Estimation

Since each stage of our stepwise inversion approach (1-D inversion, 3-D inversion, and hypoDD) relocates hypocenters, we must start this section by discussing how the location uncertainties are computed in each case. This is important because there are slight differences in how hypocentral errors are calculated at each step. In general, the errors are estimated based on the solution misfit, that is, the traveltime residuals. These residuals include both picking errors and errors associated with unmodeled velocity structure, and there is no simple way to separate these two sources (Lienert & Havskov, 1995). Compared to the 1-D inversion, it is clear that the 3-D inversion reduces significantly the occurrence of unmodeled velocities and thus reduces their effects, while the double-difference scheme attempts to eliminate altogether the influence of the velocity model by computing the relative earthquake locations within clusters.

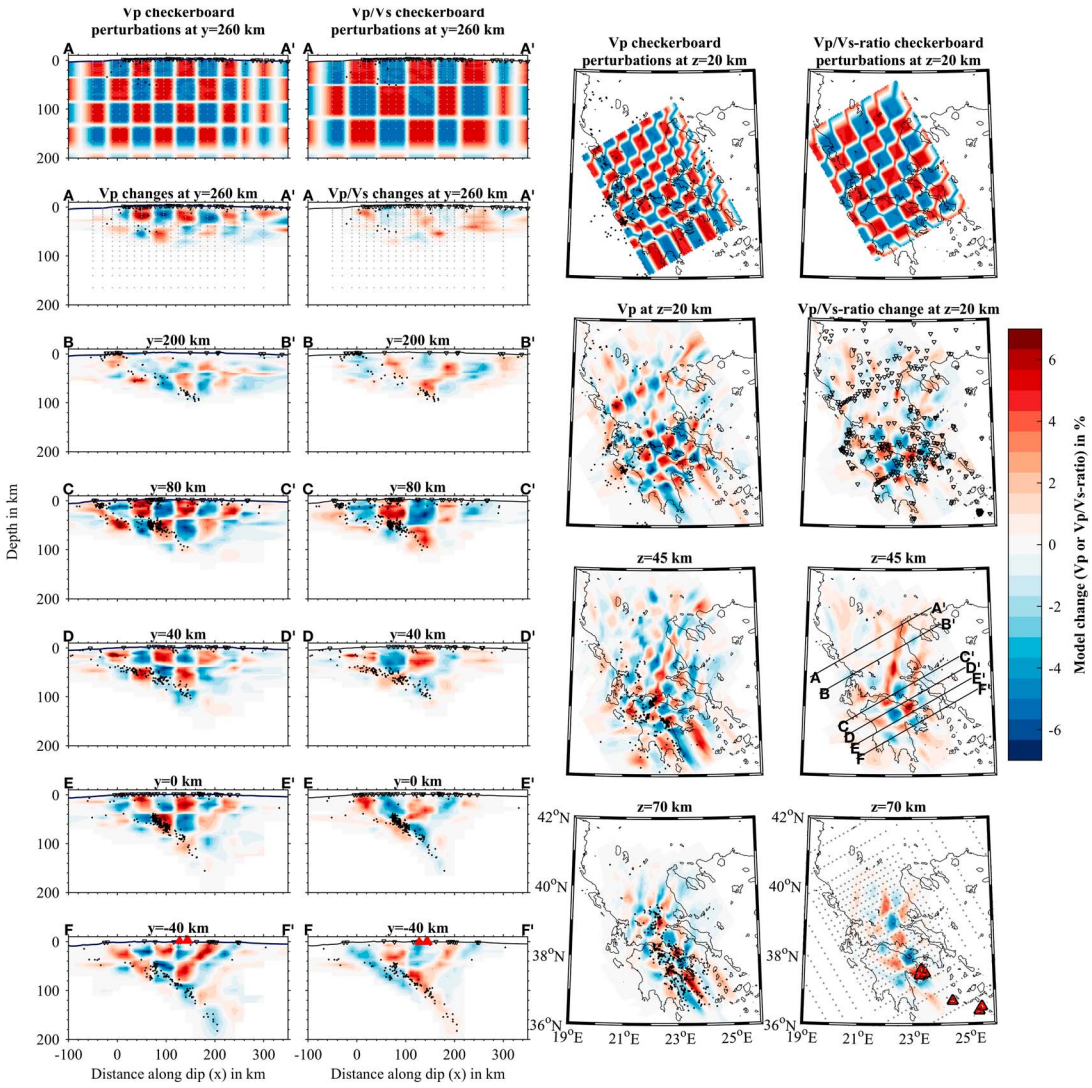

Figure 2. Checkerboard recovery test for *P* velocities and Vp/Vs ratios, shown along cross-sections A to F and at three horizontal depths slices. The uppermost row shows the input perturbations used for the calculation of the synthetic data. The inversion grid shown on cross-section A and depth slice for 70 km (small gray dots) is the same for all other sections. Station and cross-section locations are displayed on the z = 20 km and z = 45 km horizontal depth slices, respectively.

In all steps, the errors are calculated from the outer product of an SVD-derived general inverse operator and the estimated variance

$$e_i^2 = C_{ii} \cdot {\sigma_d}^2, \tag{3}$$

where e_i is the error of the i*th* parameter, C_{ii} is the outer product of an SVD-derived general inverse operator, and ${\sigma_d}^2$ is the data variance. What differs from one stage to the other is how the data variance is estimated. In the 1-D inversion, it is calculated a posteriori from the solution misfit (Lienert & Havskov, 1995)

$${\sigma_d}^2 = \frac{S^2}{(n-m)}, \tag{4}$$

where the solution misfit, S, is the sum of the weighted traveltime residuals, n is the number of observations, and m is the number of degrees of freedom. In the 3-D inversion, the data variance includes an a priori estimate based on the picking error in addition to the solution misfit (based on HYPOINVERSE; see Klein, 2002)

$${\sigma_d}^2 = e_{\mathrm{rd}}^2 + c_{\mathrm{err}} \cdot {\mathrm{rms}_d}^2, \tag{5}$$

where e_{rd} is the picking error, rms_d is the RMS of the weighted data residuals, and c_{err} is a weighting parameter (Klein, 2002) which allows to adjust the influence of errors due to unmodeled velocity structure.

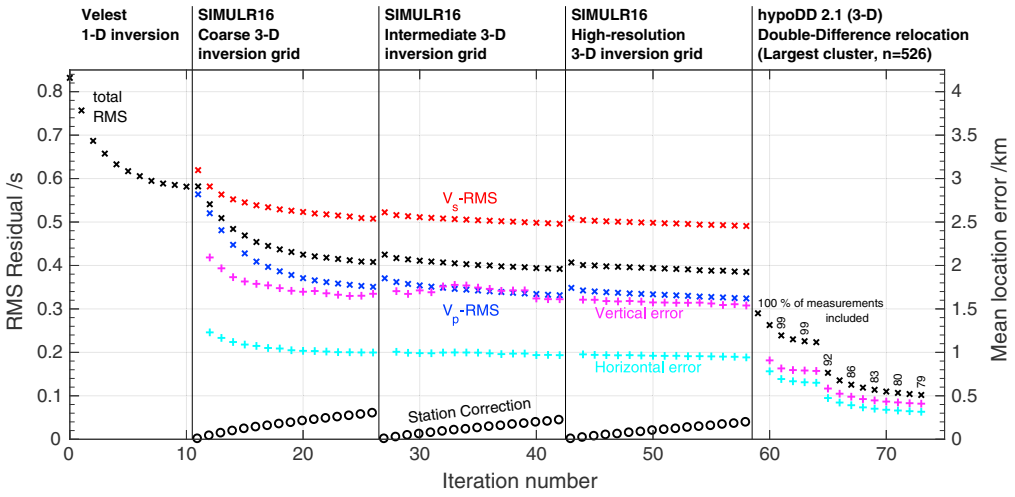

Figure 3. Reduction of root mean square (RMS) traveltime residuals and hypocenter errors for each iteration of 1-D inversion (stage 1), 3-D inversion (stage 2), and double-difference relocation (stage 3). The 3-D inversion is done for three successively denser grids, as discussed in section 3.2. Double-difference results are shown for the largest cluster of seismicity (n = 526 earthquakes) found by hypoDD. The percentages indicate the share of differential traveltimes that are included in each iteration of the hypoDD relocation.

Assuming that the 3-D inversion reduces that influence considerably, we choose a weighting parameter of 0.5 in accordance with Evans et al. (1999). This choice ensures that hypocentral errors still depend on how good the fit to the data is, while preventing reading errors to be mapped into the hypocentral error twice. In hypoDD, the variance is calculated solely based on the RMS of the weighted data residuals for differential traveltimes (Waldhauser & Ellsworth, 2000).

Taking into account these definitions of hypocentral relocation errors, we find that our errors are reduced by approximately an order of magnitude from ≈7 km at the outset of stage 1 to ≈500 m for the best resolved cluster at the end of stage 3 (see Figure 3). The initial error is already quite small owing to our strict selection of well-locatable earthquakes for tomography. From Figure 3, we observe that the errors are reduced by approximately 25% in the 1-D inversion (stage 1), 25% in the three stages of 3-D inversion (stage 2), and a further 50% in the double difference relocation. It is important to note here that the hypocenter catalog obtained at the end of the 3-D inversion provides absolute locations, which allows us to assess where the earthquakes occurred relative to the main structures of the system (e.g., subduction interface, subducted Moho). Double-difference relocation, on the other hand, improves the relative hypocenter accuracy and gives us an idea of the finer structures (e.g., active faults) along which these earthquakes occur.

As described in equation (4), the hypocenter errors calculated in the 3-D inversion depend on an assumed picking error, which we set at 0.2 s based on our manually picked arrivals and previous applications of the SIMULR package (see section 4). But since there are inconsistencies >0.2 s between our manual picks and ISC/NOA picks, we must assess the effects of considering larger picking errors. We find that a doubling of the picking error results in hypocentral errors 1.5–2 times larger than those presented above. At the end of the 3-D inversion, the estimated hypocentral errors for e_{rd} = 0.2 s are 1.5 km in the vertical direction and 1 km in the horizontal direction, which would be doubled to 3.0 km and 2.0 km for e_{rd} = 0.4 s. However, even with these conservative estimates, we should be able to determine where the earthquakes occurred relative to the main structures of the system, which are resolved with a similar degree of resolution by teleseismic scattered wave imaging (Pearce et al., 2012; Suckale et al., 2009).

6. Inversion Results

In this section, we first describe the new 1-D velocity models of the WHSZ generated by our analysis and compare them to our starting 1-D model. Then, we present the 3-D velocity models and relocated hypocenters for western Greece, focusing on the features that are deemed robust based on our resolution tests (see section 5.1 and supporting information).

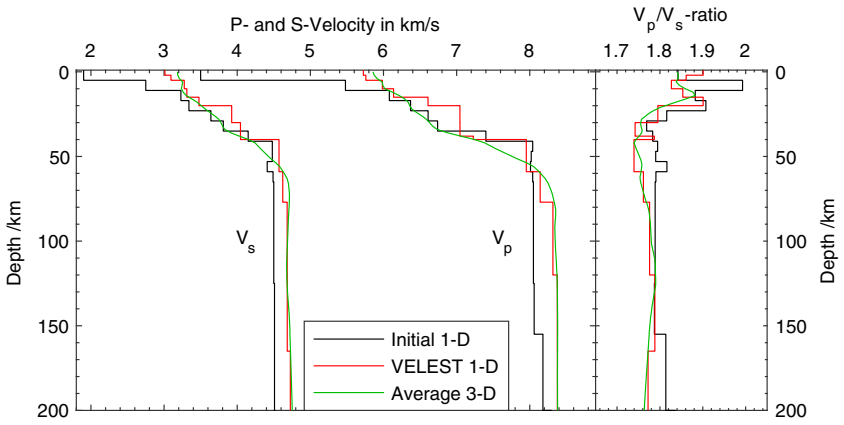

Figure 4. Comparison of 1-D velocity models. "Initial 1-D" denotes the initial model based on the model of Haslinger et al. (1999) for the crust and the AK135 model (Kennett et al., 1995) for depths below 45 km. "VELEST 1-D" is the final model based on the 1-D inversion done with program VELEST (Kissling et al., 1994) in stage 1. "Average 3D" is a 1-D velocity model constructed by taking a depth-averaged model through the final 3-D velocity model obtained at the end of stage 2.

6.1. Velocity Inversion

6.1.1. One-Dimensional Velocity Models

Our analysis workflow generates two new 1-D velocity models for the study area: (i) a layered model obtained by the 1-D inversion in VELEST at stage 1 and (ii) a model calculated by averaging velocities within depth slices through the final 3-D velocity model obtained at stage 2. These new models are plotted in Figure 4, in conjunction with the starting 1-D model that was used for the inversion (see section 3.2). Compared to the starting model, our new layered 1-D velocity model exhibits more pronounced velocity gradients at layer boundaries, especially at 15 km to 20 km and 38 km to 40 km depths, with velocities that are greater in the upper crust and comparable in the lower crust. Velocities in the upper mantle are 3% to 7% higher than those from the AK135 model, something that might be due to the existence of a cold (i.e., fast) dipping slab across a large portion of the imaged volume. For its part, the depth-averaged 1-D model tends to follow more closely the starting model in the crust and the new 1-D layered model in the mantle (with velocities higher than AK135). But in contrast to both the starting and the new 1-D layered models, the depth-averaged model is very smooth, reflecting the fact that it averages over laterally variable structures associated with the subduction system.

6.1.2. Three-Dimensional Velocity Models

The results of our 3-D local earthquake tomography of western Greece are presented as trench-normal vertical sections (A-A′ to F-F′, Figures 5 and 6) and horizontal depth slices (15 to 80 km depth, Figures 7 and 8) through the final Vp and Vp/Vs ratio models (a set of trench-parallel sections is also shown in Figure S6 of the supporting information). The Vp model shows a dichotomy between a low-velocity upper layer representing generally the overriding crust (top layer, 0 km to 40–60 km, Vp< 7.5 km/s) and a high-velocity lower layer representing the mantle (bottom layer, Vp> 7.8 km/s on average). The interface between crust and mantle is not as clear in the Vp/Vs model, but the upper crust exhibits generally higher Vp/Vs ratios (1.85 to 1.95). Five outstanding features of interest in the velocity models are marked with roman numerals I–V in Figures 6–8.

1. A localized thickening of the top layer down to ≈60 km depth within the collision zone, with a rapid thinning to ≈35 km depth on both sides. North of the KTF (cross-sections A and B), this feature appears to be offset by 40 km toward the backarc relative to its southern counterpart (c.f., cross-sections C-F).
2. A low-Vp (7.0–7.8 km/s) layer dipping at 20° toward the NE and extending from 40 km to up to 90 km depth. This low-Vp layer appears most clearly in the center of the imaged domain (sections C-E) but is generally visible in all the cross sections. To the north, the velocity contrast marking the top of the layer becomes less sharp, but the bottom of the layer remains clearly demarcated from the underlying higher-velocity mantle (see, e.g., Figure 6 B). Below the central and southern Peloponnesus (6 E-F), the low-Vp layer appears somewhat interrupted at 60 km depth.

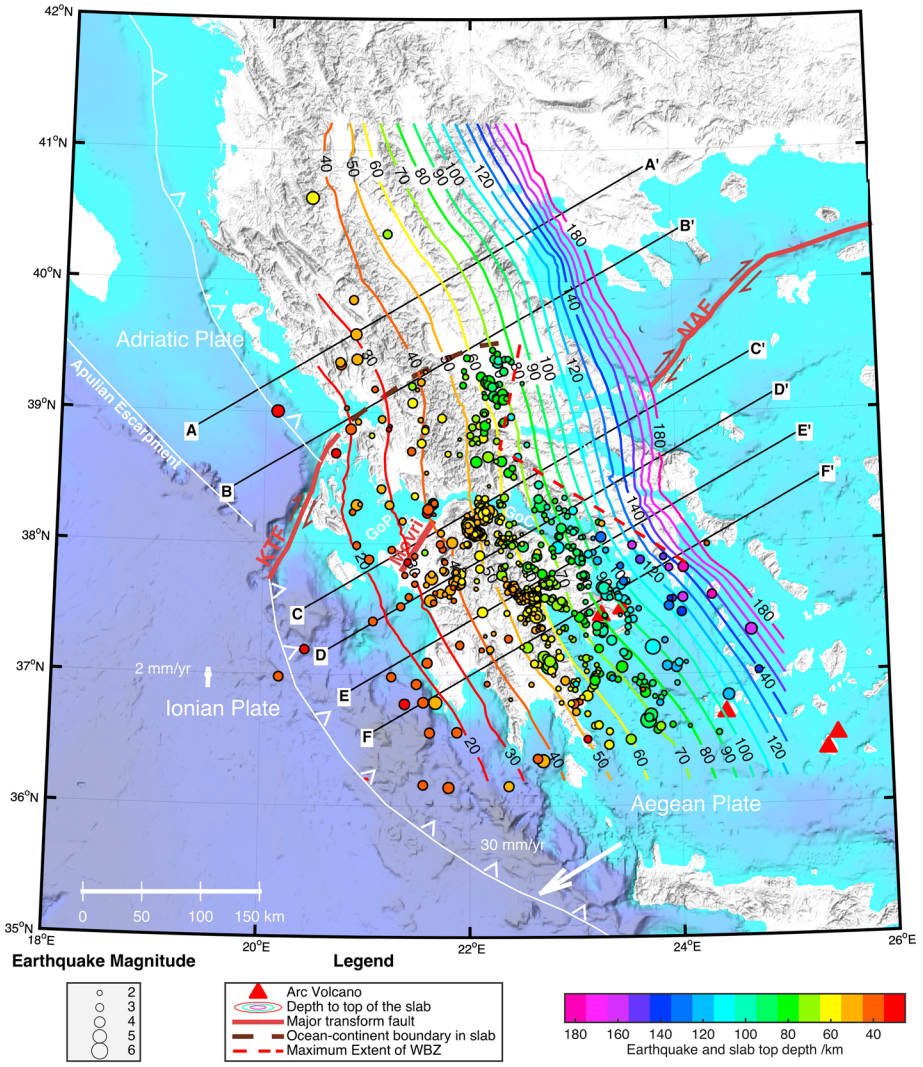

Figure 5. Map of mainland Greece and the Western Hellenic Subduction Zone showing the locations of cross sections and relocated hypocenters. Parallel black lines with labels A-A′ to F-F′ indicate the locations of the cross sections through the final 3-D velocity models shown in Figure 6. Colored circles represent earthquakes with depths greater than 25 km that were relocated in this study. The circles are color coded by depth, and their size is proportional to earthquake magnitude. See legend for the description of other symbols and lines.

3. A high-Vp (8.4 km/s to 8.9 km/s) dipping layer directly underlying the low-Vp dipping layer described in the previous point. This layer is observed from 50 km to 180 km depth and appears to extend beyond the bottom of the imaged volume.
4. A low Vp/Vs ratio anomaly (down to ≈1.64) located mainly in the lower part of the overriding crust, with some excursions into the mantle wedge and upper crust. It stretches 75 km from the suspected plate interface toward the arc and is ≈15 km thick where sharply imaged. The contrast between the anomaly (low Vp/Vs) and the upper crust (high Vp/Vs) is greatest below the northwestern Peloponnesus (Figure 6 C and D).
5. A high Vp/Vs ratio anomaly (up to ≈1.85) located just above the WBZ in the southern sections (C-F). The feature has the largest amplitude in section E, below the central Peloponnesus, and extends all the way to the southern boundary of the study area.

Features VI–VIII are addressed in the description of hypocenters and in section 7.

6.2. Hypocenters

The earthquakes that were relocated beneath the WHSZ as part of this study are shown in Figure 5 (full set in map view), Figure 6 (subsets in cross sections), and Figures 7 and 8 (subsets in horizontal depth slices).

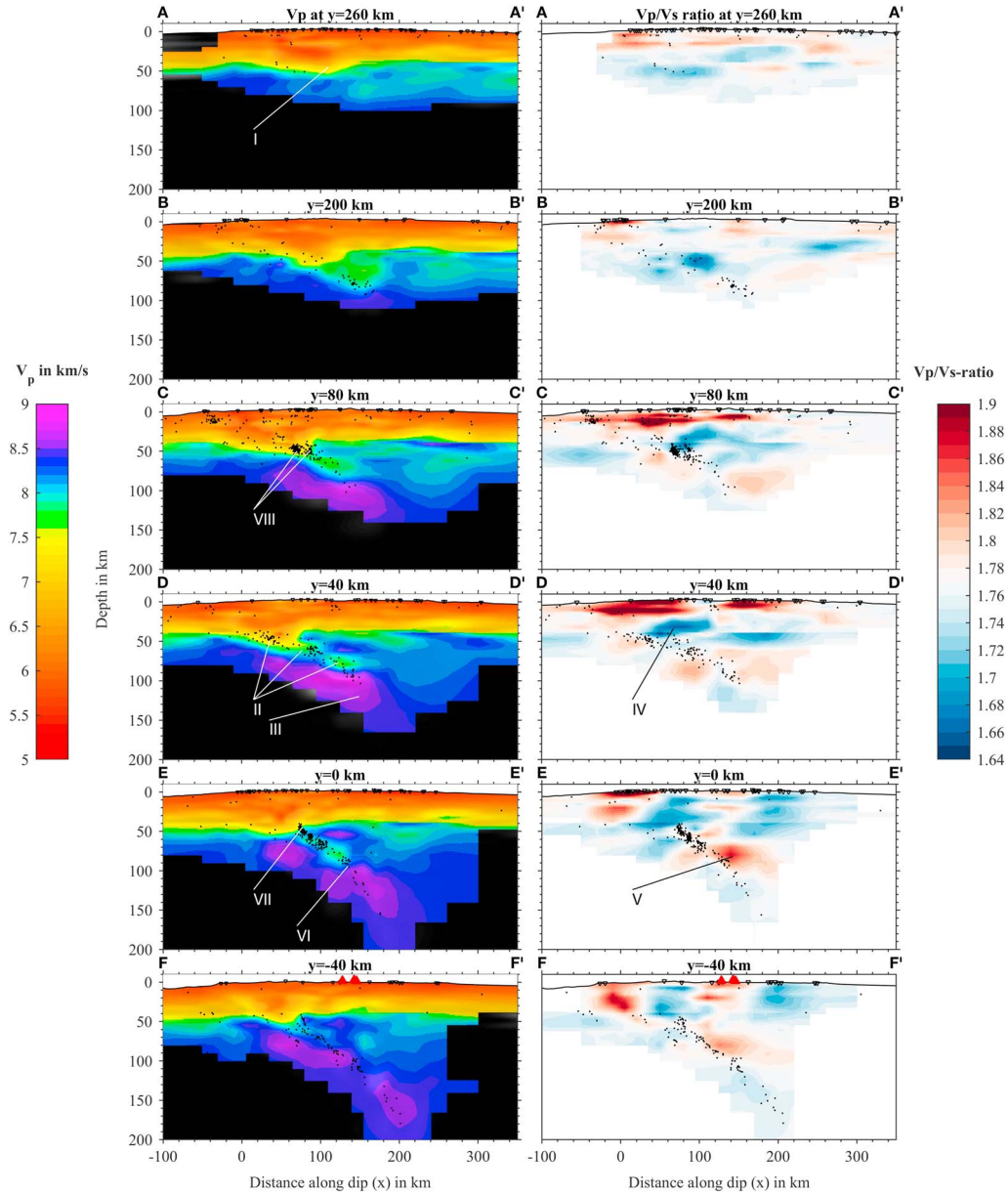

Figure 6. Cross sections through the final 3-D Vp and Vp/Vs ratio models. Locations of the cross sections are indicated in Figure 5, and the reference axes for the coordinate system (*x*,*y*) are shown in Figure 1. Black dots represent relocated hypocenters at two different stages of the analysis: the left column shows hypocenters after double difference relocation (stage 3), whereas the right column shows hypocenters after 3-D inversion of traveltimes (stage 2; see Figure S2 for a further comparison of hypocenters during each stage).

All these maps and cross sections show earthquake locations obtained at the end of stage 3 in our analysis workflow (i.e., double-difference relocation), except for the cross sections in the right column of Figure 6, which shows earthquake locations obtained after stage 2 (3-D inversion). The reason for showing hypocenters from stages 2 and 3 side by side is to assess the improvements associated with double-difference relocation (all incremental differences from before stage 1 to after stage 3 are described in the supporting information, with Figure S2 showing earthquake locations and hypocentral errors from each stage). When comparing the left and right columns of Figure 6 (see also Figure S2), we note that the improvements in relocation due to hypoDD relocation are subtle, that is, the overall hypocenter distribution looks very similar compared to stage 2, but closer inspection reveals that the double-difference relocation tends to collapse clouds of earthquakes into more confined planes of seismicity (likely representative of faults).

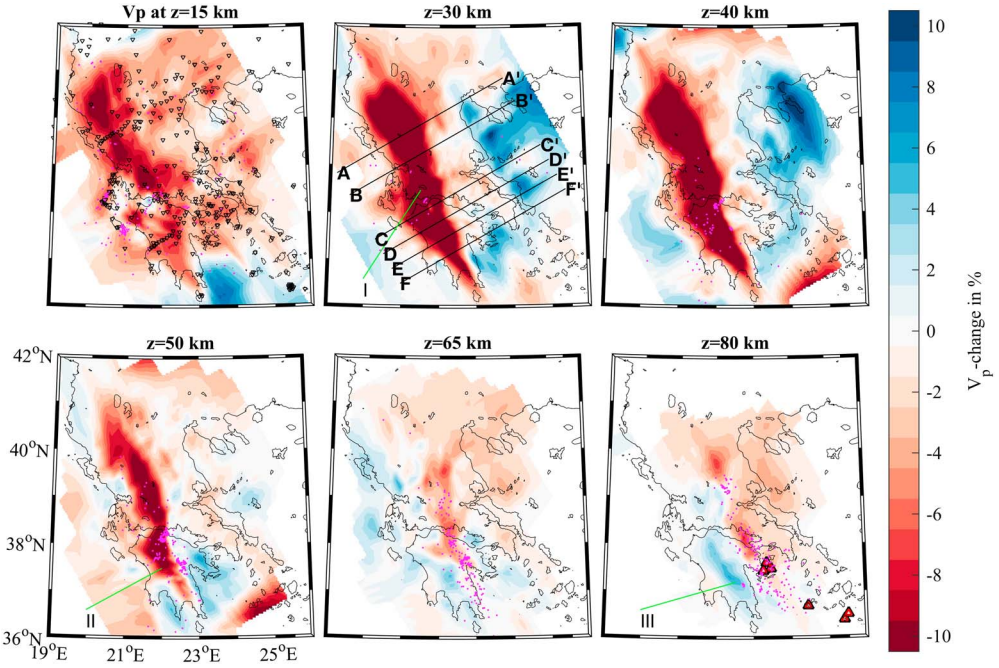

Figure 7. Horizontal depth slices through the final 3-D Vp model with superimposed seismicity. Magenta dots indicate hypocenters relocated by double difference within each depth slice. Black lines mark the locations of the cross sections shown in Figure 6, for comparison. The large, coherent low-velocity feature is interpreted as the subducting crust dipping toward the NE. It is deformed at 38°N, probably due to a higher rate of rollback in the south compared to the north. Here we chose to plot velocity perturbations to highlight imaged structures. For direct comparison with cross sections, depth slices showing absolute *P* velocities are presented in Figure S7 of the supporting information.

From Figures 5 and 6, we note that the relocated earthquakes form a relatively narrow dipping band which follows the expected path of the subducted slab and thus outlines a well-defined WBZ in the southern portion of the system. This WBZ reaches a maximum depth of 185 km in the south, beneath the Cyclade Islands. In this southern part of the model, there is an apparent bend in the WBZ at 80 km, marking a dip increase from 20° above to 60° below (see feature VI in Figure 6). Simultaneously, the WBZ becomes thinner below that bend. Moving northward, the lower end of the WBZ rises progressively to a minimum depth of 60–70 km beneath a region encompassing the Gulf of Corinth and the Northern Gulf of Evia, before it plunges again toward the north, forming a V-shaped gap in deep seismicity (see red dashed line in Figures 5 and 11). Below this central region, the WBZ also appears to migrate slightly toward the backarc from south to north (compare profiles C and B in Figure 6). We observe a possible bend of the WBZ at ~60 km depth in profile C (i.e., shallower than to the south), but this feature is not well constrained due to the limited number of earthquakes outlining the deeper segment of the WBZ. Farther north, the well-defined WBZ disappears almost completely and quite abruptly along a SW-NE line coinciding with cross-section B in Figure 5. Beyond this point, only a handful of intermediate depth events have occurred during the time period of our study.

Within the region where the WBZ is well defined, two earthquake clusters stand out from the general intraslab seismicity. The first cluster is located directly below the southern receiver function migration line (feature VII, in section E of Figure 6). In this cluster, earthquakes form a rough plane that has a dip of ≈60° and extends above the low-velocity layer, between 40 and 60 km depth. There is very little intraslab seismicity trenchward of this cluster. The second cluster is located beneath Leontio in the northern Peloponnesus (feature VIII, in section C of Figure 6). This cluster is more cloud shaped than the first one and appears to be divided into two subclusters. It has a height of 20 km, a width of 30 km, and extends from 40 km to 60 km depth. We also note that it is located near the apex of the V-shaped seismicity gap discussed above (see Figure 5).

7. Discussion

In this section, we interpret our velocity models and relocated earthquakes in conjunction with previous seismic results obtained in the region. We rely particularly on constraints provided by the high-resolution 2-D

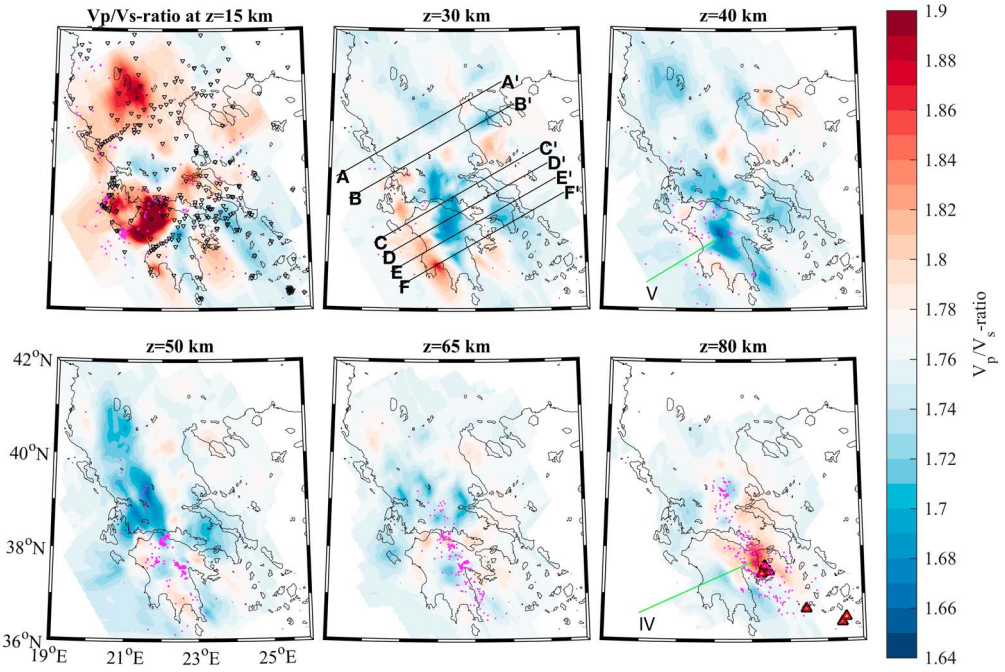

Figure 8. Horizontal depth slices through the final 3-D Vp/Vs ratio model with superimposed seismicity. Magenta dots indicate hypocenters relocated by double difference within each depth slice. Black lines mark the locations of the cross sections shown in Figure 6, for comparison. The high Vp/Vs ratio anomaly centered below the Saronic Gulf at 80 km depth might represent hydrated, partially melted material in the mantle wedge which feeds the overlying volcanic arc (red triangles). Regions of low Vp/Vs ratios occur in the overriding forearc crust (see, e.g., anomaly labeled V), especially to the north of 38°N (at 50 km depth).

images from scattered teleseismic waves, obtained by Suckale et al. (2009) and Pearce et al. (2012) with an inversion technique based on the Generalized Radon Transform (GRT-RF). Side-by-side comparisons and maps integrating the various results are shown in Figures 9–11. Figure 9 shows both the tomographic Vp model and GRT images, which we remigrated with the depth-averaged 1-D velocity model from this study (Figure 4). Compared to the previous images of Pearce et al. (2012), the only change is an upward shift of the slab structure by up to 3 km. From the tomographic models, the GRT-RF images, and from the 3-D receiver function

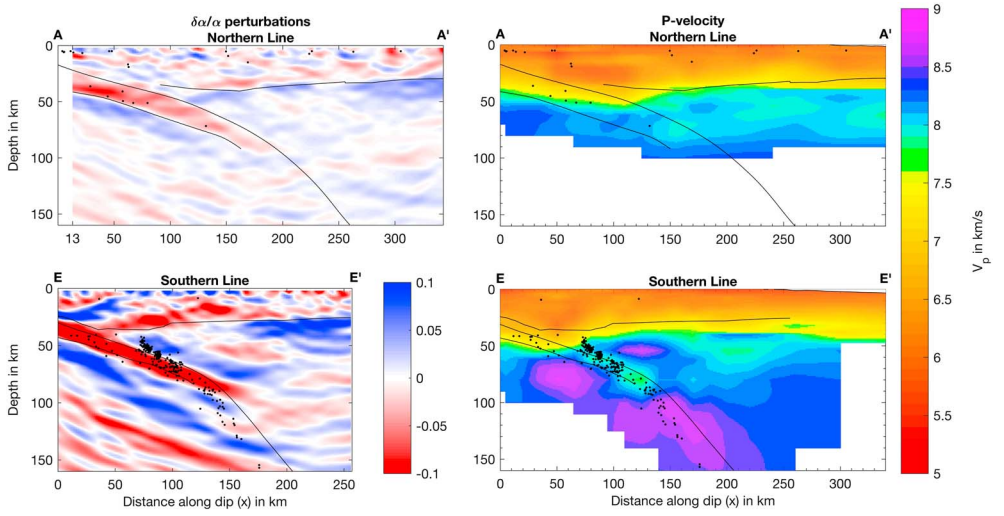

Figure 9. Comparison of Generalized Radon Transform images (Pearce et al., 2012) and tomographic models along the northern and southern lines of the MEDUSA experiment. Only *P* wave scattering potential ($\delta\alpha/\alpha$) and *P* velocities are plotted, together with earthquakes relocated by double difference. The black solid lines indicate the interpreted overriding Moho, slab top, and subducting Moho.

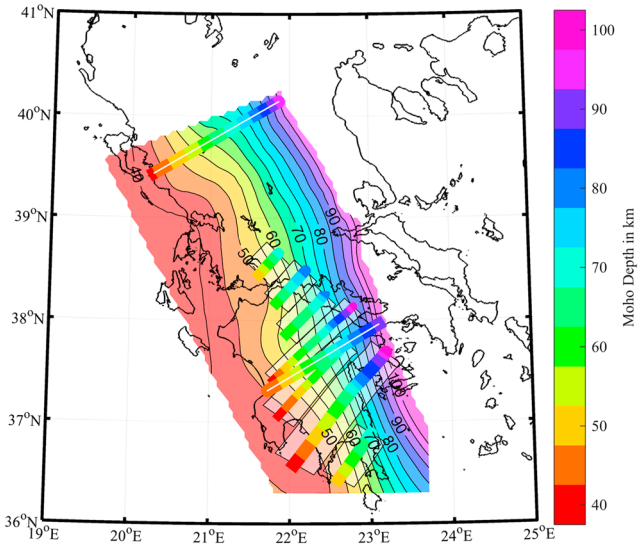

Figure 10. Depth contours of the subducted Moho from 3-D tomography and comparison with previous receiver function studies. The background contours and color map indicate the depth to the subducted Moho from our resulting 3-D Vp model. The light, transparent boxes overlaying the base map show subducted Moho depths from the 3-D receiver function study of Sachpazi et al. (2016), while the boxes with white lines (one in the south and one in the north) show the subducted Moho depth from the Generalized Radon Transform images of Pearce et al. (2012). A comparison of the various results reveals deviations that are generally less than $\pm 5km$, except for a few receiver function profiles from Sachpazi et al. (2016) which show a subducted Moho that is ≈10 km deeper beneath the Gulf of Corinth.

study of Sachpazi et al. (2016), we picked both the subducting Moho and the slab top (where possible). In Figure 10, we show that the new estimate of the subducting Moho fits these studies within approximately 5 km (vertically). Figure 11 depicts a common model of the subduction interface geometry in 3-D. We then interrogate these integrated seismic models to gain new insight into the relationships between the ocean-continent transition and the structure, dynamics, and seismicity of the WHSZ.

7.1. Subducting Crust and Seismicity

We interpret the dipping low-velocity layer observed across our models (Feature II; see section 6) and the GRT profiles as the hydrated, basaltic oceanic crust. We note that the tomographically derived velocities of 7.0 km/s to 7.8 km/s may seem high for hydrated oceanic crust, but they probably represent lower velocities that have been smoothed and smeared by the tomographic inversion. The layer disappears at a maximum depth of 90 km, where the crust likely transforms into eclogite. During eclogitization, the subducting crust loses its velocity contrast in comparison with the underlying subducting mantle and the overlying mantle wedge (Figure 6, features II and V). The apparent termination depth of 90 km is very similar to that found by Pearce et al. (2012) and Sachpazi et al. (2016), where the subducting crust or Moho, respectively, could be imaged to about 100 km depth. Below this depth, earthquake hypocenters occur along a much steeper trend of 60°. This agrees well with the results of Papazachos et al. (2000) where a bend in the WBZ is inferred at 100 km depth. Imaging this bend in the slab structure has proved challenging, as shown by both the weak recovery of velocity contrasts below 90 km in this study and the RF studies of both Pearce et al. (2012) and Sachpazi et al. (2016). The velocity contrast along a steeply dipping slab is hard to recover with RF techniques due to the conflict between the limited aperture of the seismometer arrays and the wide-angle conversions along steeply dipping features (MacKenzie et al., 2010). While Sachpazi et al. (2016) place the slab bend at 60 km depth, Pearce et al. (2012) do not capture any bend in the slab down to the termination of the LVL at 100 km. Although recovery of structures through tomography is also hampered at this depth due to the ray coverage and source distribution (as shown by the checkerboard tests), our images do show a velocity contrast following the steepening trend of the WBZ down to 150 km depth and beyond. This increase in velocity from the mantle wedge to the slab across this trend suggests that we do recover some slab structure reflecting the eclogitized crust below 90 km. Thermal-petrological models predict that the basalt-eclogite transition occurs over a large depth range (van Keken et al., 2012) so we would perhaps expect a more progressive fading of the LVL here. However, imaging a thinning and hydrated subducting crust is challenging when the slab steepens at the same time.

Previous regional and teleseismic tomographic models (Koulakov et al., 2009; Piromallo, 2003; Spakman et al., 1988; Zhu et al., 2015) suggest a general slab dip of 45° below 100 km. This contrasts with our observation of the 60° dip for the deep part of the WBZ. While the thinning and steepening of the WBZ may be due in part to the bending of the slab, it also suggests that seismicity follows a path that is deeper in the slab and oblique to the subduction interface at this depth. This path could follow the phase boundary between blueschist and eclogite, which can result in a thinning of the seismic zone as shown by van Keken et al. (2012). Upon complete eclogitization of the crustal material, there is much less fluid available beyond that depth, which limits the potential occurrence of dehydration embrittlement and associated intermediate depth earthquakes (see Figure 12). The shape of this phase change is a result of the subducting crust being heated from the top; thus, material closer toward the bottom of the subducting crust only reaches the temperatures required for the phase transition at greater depths. It is not perfectly understood why the steepening of the slab occurs at eclogitization depth, but this phenomenon has been observed in many subduction zones and may be related to the sudden density increase at that depth (Klemd et al., 2011). While the thinning of the WBZ occurs over a depth range between 80 km and 180 km in the south, this depth range is much shorter north of the Gulf of Corinth: instead of thinning out, seismicity is more intense at a depth of 90 km. This clustering of the deepest intermediate depth seismicity has been observed in Japan, where Nakajima et al. (2013) postulated

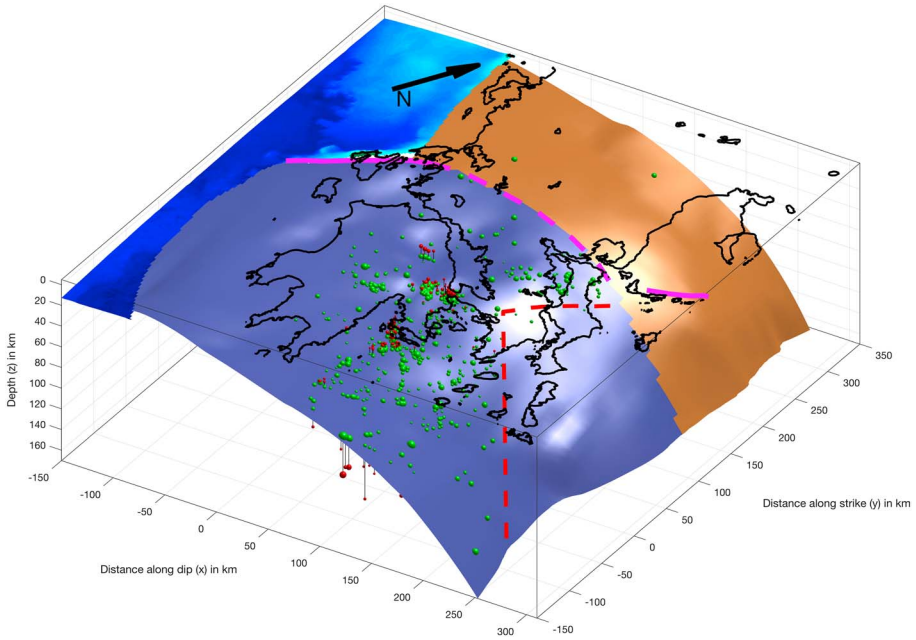

Figure 11. Three-dimensional block model of the subduction interface and seismicity based on the results obtained in this study. The subducting oceanic crust of the Ionian plate is dark blue, while the subducting continental crust of the Adriatic plate is in brown. Variable shading on the interfaces represents relief, with oblique illumination from a light source to the right of the model. The magenta solid lines mark large strike-slip faults, including the Kephalonia Transform Fault and the western tip of the North Anatolian Fault. The magenta dashed line marks the putative boundary between oceanic and continental slabs based on the contrast in seismicity (though apparent changes in the slab's tomographic response could also be used to constrain this boundary, we refrain from doing so as there is a progressive change in resolution associated with the contrast in seismicity between north and south; see Figure 2). Relocated hypocenters are indicated by red spheres, with size corresponding to magnitude. The green spheres are hypocenters projected onto the slab top surface. Red dashed lines indicate the outline of a V-shaped seismic gap believed to be associated with a broad zone of deformation in the oceanic slab.

that the cause may be the differential stresses induced through the volume change which accompany the basalt-eclogite transition. These different styles in the termination of the WBZ across the study region likely show that the thermal state of the subducting crust varies considerably between the south and north.

Earthquakes in this region occur along a thin, single-planed WBZ (instead of a double seismic zone) and are largely restricted to the southern part of the system. Nearly all the earthquakes map directly into the low-velocity subducting crust. Seismicity within the subducting mantle is nearly absent, but a few such events do occur in the south of the imaged domain (Figure 6 cross-section F). In this region south of mainland Greece, biased station coverage might have caused an increase in depth errors. If these are true mantle earthquakes, occurring below the main plane of seismicity within the subducting crust, this second plane would be offset by only ≈12 km. Since double seismic zones are generally expected to have a separation distance of more than 35 km (Brudzinski et al., 2007) for a plate age such as the Ionian of 230 Ma (Speranza et al., 2012), we assume that the WBZ in our study region consists of only one plane of seismicity (equivalent to the upper plane of a double seismic zone).

Along strike of the subduction zone, seismicity decreases abruptly toward the north, along a trench-perpendicular line extending from the KTF toward the backarc (see map of relocated seismicity in Figure 5). Deep earthquakes are nearly absent north of that line. However, there are a few robustly located earthquakes that occur between 40 km and 70 km depth in the Adriatic subducting crust (see the nine earthquakes with depths >40 km observed north of line B-B′ in Figure 5). The existence of these earthquakes lends independent support to mounting evidence that active subduction is currently taking place north of the KTF. As the KTF marks the boundary between drier continental crust in the north and wetter oceanic crust in the south, we can further hypothesize that the difference in composition and metamorphic state of the subducting crusts might be responsible for the aseismicity in the north. The GRT image in Figure 9 A shows

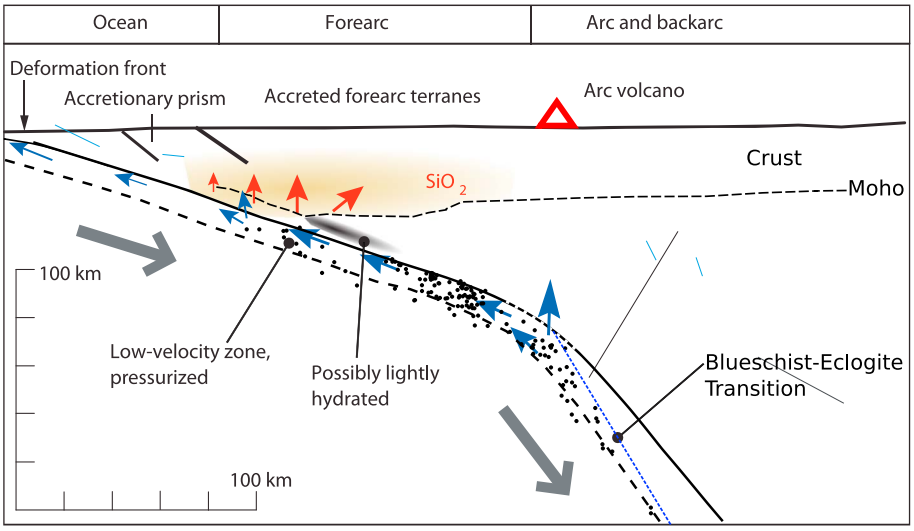

Figure 12. Conceptual model of quartz enrichment in the overriding lower forearc crust in Greece, after the model proposed for Cascadia by Audet and Bürgmann (2014). Compared to Cascadia, the Western Hellenic Subduction Zone is a much colder subduction zone. That means that the subducting crust is dehydrated and transformed to eclogite at larger depths. It also leaves a larger piece of intact, impermeable subduction interface to guide fluid migration to the forearc. Thus, less mantle wedge hydration and more quartz enrichment in the forearc occur.

that the low-velocity layer extends to 90 km depth (as imaged by *P* wave scattering potential), some 20 km below the deepest earthquakes in the north. That could imply that unmetamorphosed crust is stable to depths beyond where earthquakes occur, possibly because there is not enough water to facilitate prograde metamorphism (Austrheim, 1987) and trigger earthquakes.

The two intense clusters of seismicity (Figure 6 features VII and VIII and Figure 9) that stand out above the average WBZ seismicity are striking, because they seem to occur within and up to 15 km above the subducting Ionian crust (see Figure 6 C, E). This would mean that some of these earthquakes occur in the mantle wedge, which is not expected from the current models for intermediate depth seismicity. Even though the mantle wedge is usually assumed aseismic, we note that earthquakes within the mantle wedge have been discussed in Japan (Uchida et al., 2010) and New Zealand (Davey & Ristau, 2011). In Japan, it has been suggested that earthquakes occur in detached, subducted seamounts (Uchida et al., 2010). In New Zealand, it has been hypothesized that earthquakes are associated with the boundary of the serpentine stability field within the mantle wedge (Davey & Ristau, 2011). At this point, we are unable to say whether these clusters indicate one or another of these processes, but the matter is the subject of ongoing work.

7.2. Fluid Flux and Metasomatism

Now that we have established where the dehydration and eclogitization of the slab occur based on our Vp models; we can look into what happens to the released fluids and the effect they have on the composition of the mantle wedge and the forearc crust. To do this, we focus on Vp/Vs images, as these are particularly sensitive to variations in porosity, fluid/melt content, and fluid pressure (Unsworth & Rondenay, 2013).

7.2.1. Evidence for Free Fluids or Melt

High Vp/Vs ratios are indicative of water-rich fluids or melts. We find a high Vp/Vs ratio in one location in the subarc mantle wedge, clearly limited to along the strike of the subduction zone (Figure 6 V). Within this part of the subduction zone, right above the slab at 80 km depth, the Vp/Vs ratio increases to 1.86 from an average of 1.77. This anomaly coincides with the disappearance of the low-velocity subducting crust (II) and the bend of the WBZ (VI) throughout the southern part of the slab. The variable amplitude of this anomaly along strike of the WHSZ suggests that dehydration and fluid flux vary strongly along strike as well. As the Quaternary volcanic arc of the WHSZ does not continue north of where the anomaly appears strongest, we suspect a possible correlation between the amount of slab dehydration and volcanism in this area. However, we do note that active eclogitization reflected in deep earthquake clusters also occurs farther north, which would release

fluids in areas where we do not image high Vp/Vs anomalies. We do not know what happens to these fluids in the north; they are possibly released at depths where the mantle wedge is too cold to allow melting, but both the hydration of the cold mantle wedge corner and updip migration through the subducting crust are possible scenarios.

7.2.2. Hydration of the Mantle Wedge Corner

Where temperatures are too low for dehydration-derived fluids to fuel melting below the arc, fluids might either hydrate the cold mantle wedge corner or migrate farther updip. During hydration of the cold mantle wedge corner, chlorite and serpentine in particular are formed. These exhibit high anisotropy, low density, low seismic velocities, and high Vp/Vs ratios in comparison to mantle peridotite.

Evidence for serpentinization has been found for the cold corner of the Hellenic mantle wedge (Olive et al., 2014; Sodoudi et al., 2015). But unlike more extreme cases such as Cascadia, where serpentinization is so extensive that it causes an inversion of the Moho seismic impedance contrast (Bostock et al., 2002), the WHSZ exhibits only moderate signs of serpentinization. Indeed, the GRT images of Suckale et al. (2009) and Pearce et al. (2012) found only a small weakening in the Moho's signal above the mantle wedge beneath the Peloponnesus. The pattern of seismic anisotropy within the backarc that Olive et al. (2014) recovered supports at least a thin layer of serpentine at the top of the subducting crust. Our results show low velocities only within the very tip of the mantle wedge when we assume the wedge's location from Pearce et al. (2012; see Figure 9). The resolution of our tomography is likely inferior to the GRT images, and the low velocities could be smeared between the thickened overriding crust and the subducting crust. However, the Vp/Vs ratio shows locally pronounced, low values of 1.65 within the lower overriding crust, stretching into the cold corner of the mantle wedge. These low Vp/Vs ratios are not compatible with a dominant presence of serpentine, and neither is *P* velocities above 8 km/s, which are typical of mantle peridotite. The high velocities thus indicate a rather dry mantle wedge corner. This fits well with a recent estimate of less than 5% mantle wedge hydration for the Hellenic, and many other comparable subduction zones, based on their water budget (Abers et al., 2017).

7.2.3. Silica Enrichment of the Lower Forearc Crust

In our tomographic model, the low Vp/Vs feature (Figure 6 IV) extends from the subduction interface toward the arc, suggesting that the lower crust has been altered by subduction-derived material. With its low bulk Vp/Vs ratio and Poisson's ratio, quartz is the most likely abundant mineral to explain an exceptionally low bulk Vp/Vs ratio over such a large region (Hyndman et al., 2015). This kind of silica enrichment has been proposed based on similar tomographic evidence for the Cascadia subduction zone by Ramachandran and Hyndman (2012). According to the conceptual model of Audet and Bürgmann (2014) and Hyndman et al. (2015), large quantities of quartz (possibly even its β phase) are precipitated in veins in the lower overriding crust by fluids that are derived from the subducting crust and migrate updip. This updip migration path may be particularly favored over migration to the mantle wedge in the case of an undamaged, impermeable interface. Precipitation is thought to occur at the interface between the subducting and overriding crust, which exhibits a higher permeability than the deeper subduction interface below the mantle wedge. A possible field analog has been described by Breeding and Ague (2002) in New Zealand. There, large amounts of quartz have been precipitated in veins in a comparable, now exposed, forearc environment.

How much silica can be transported depends on silica solubility, which is controlled by temperature. An aqueous fluid in equilibrium with quartz-bearing rocks contains more silica at high temperatures than at low temperatures (Manning, 1994). But the source of quartz is uncertain. For Cascadia, Hyndman et al. (2015) suggest that both metamorphosed silt- and sand-rich rocks and metamorphosed basalts might provide soluble quartz. In comparison to unaltered basalt, metamorphosed blueschists can contain modal quartz together with low-silica minerals, according to Peacock (1993).

If the anomalous Vp/Vs ratio in the lower overiding forearc crust does indeed represent a region of silica enrichment, then it would be a considerably larger volume than has been inferred in Cascadia by Audet and Bürgmann (2014), Hyndman et al. (2015), and Ramachandran and Hyndman (2012). In the WHSZ, the low Vp/Vs ratio spans a region of up to 80 km between subduction interface and toward the arc rather than half that size as conceptualized for Cascadia. Requiring dehydration-derived fluids for the silica transport, this large area of quartz deposition in the WHSZ conflicts with the interpretation of little fluid transport to, and little hydration of, the cold mantle wedge corner.

Two causes might help explain this discrepancy of large amounts of precipitated quartz, but low mantle wedge hydration in the WHSZ (see sketch in Figure 12).

1. The WHSZ possesses an unusually large sedimentary prism, with 8 km of sediments on top of the crystalline oceanic crust, compared to a global average of 3.5 km for accretionary subduction zones (Clift & Vannucchi, 2004). Combined with a larger-than-usual thickness of subducted sediments (1 km compared to a global average of 0.3 km; Syracuse et al., 2010), there is a large source for quartz solution available. This source is notably larger than in the Cascadia subduction zone, where 2 km of sediments lies on top of the subducting plate and 0.4 km of sediments is subducted (Syracuse et al., 2010).
2. Estimates of the amount of hydration in the mantle wedge corner and of silica transport assume only vertical migration of dehydration-derived fluids. In reality, fluids might migrate considerable distances updip within the subducting crust due to an impermeable plate interface. The plate interface might be sealed where it is unaffected by metamorphic reactions that are accompanied by volume changes—particularly the blueschist to eclogite transition. In Cascadia (a hot subduction zone end member with profound mantle wedge hydration), these metamorphic reactions occur at much shallower depths and closer to the cold mantle wedge corner than in the colder WHSZ. The weak, shallow subduction interface could allow fluid migration to the cold mantle wedge in Cascadia. Meanwhile in Greece, fluid migration might be prohibited by an intact seal formed by a low-permeability plate interface reaching down to greater depths. Thus, less mantle wedge hydration but more silica transport might still be compatible.

We thus argue that fluids fluxed from the subducting oceanic crust may have transported silica to the overriding forearc crust of the WHSZ. This might have a strong effect on the rheology of the plate interface: Audet and Bürgmann (2014) showed that short recurrence intervals of episodic tremor and slip correlate with high Vp/Vs ratios in the forearc crust. Based on this relationship, we expect that episodic tremor and slip behavior would exhibit short recurrence intervals in the WHSZ. Future research will need to evaluate this prediction, as no episodic tremor and slip has been observed in the WHSZ to date.

7.3. Transition Between Continental and Oceanic Slab

Both our tomographic images and the relocated hypocenters shed light on the characteristics of the transition between oceanic subduction in the south and continental subduction in the north. These new observations, in conjunction with results from previous imaging studies, suggest that there is a sharp transition in crustal type below the KTF at depth but that the zone in which the slab is deformed due to differential rollback between south and north stretches over an area spanning the whole Central Hellenic Shear Zone (CHSZ). Here we will discuss the likely mechanisms of slab deformation in the WHSZ. We base this discussion in Figure 10, which shows the depth contours of the subduction interface, and Figure 11, which shows the spatial relation between the subduction interface and seismicity in a 3-D model.

7.3.1. Is There a Trench-Parallel Slab Tear?

A trench-parallel slab tear propagating from the north to the south has been suggested by mantle-scale tomography studies, which diffusely imaged an intermittent slab in the north (e.g., Bijwaard et al., 1998; Koulakov et al., 2009; Spakman et al., 1988; Zhu et al., 2015). The disturbance appears at a range of depths: in Spakman et al. (1988), the anomaly is discontinuous at 180 km to 250 km depth, in Koulakov et al. (2009) at 300 km to 500 km depth, and in the EU60 velocity model published by Zhu et al. (2015) at 200 km to 400 km depth. The *P* wave model of Piromallo (2003) does not show a disturbance. Spakman et al. (1988) suggest that the tear reaches the southern Peloponnesus in their model, while the model of Zhu et al. (2015) suggests that the tear affects the slab north of Greece. Based on their tomographic results, Wortel and Spakman (2000) discussed the development of slab detachment and the propagation of trench-parallel tears in the Mediterranean as a necessary consequence of the Tethys closure. They suggest that a slab tear is propagating from the north to the south, which would fit in well with the current understanding of a light, continental crust withstanding subduction in the north and a dense oceanic slab pulling in the south (Royden & Papanikolaou, 2011).

Although our tomographic study does not reach the depths of the inferred tear, we can look into our results to see if any observations are consistent or inconsistent with the presence of such a tear. Hypothetically, the termination of slab seismicity could mark the location where the deeper slab has been detached. Detaching the slab would remove slab pull forces which might be required for intraslab earthquakes. With the disappearance of slab pull, rollback should stop where the slab is detached—which is the case in northern Greece.

However, the pattern of intermediate depth earthquakes and the geological history of the KTF are not consistent with being directly affected by a trench-parallel slab tear. First, seismicity within the subducting crust up to the KTF is well distributed, while one would expect to find earthquake clusters and swarms in regions where the slab tear is propagating (Meighan et al., 2013). Neither seismicity, focal mechanisms nor a σ_3-axis subparallel to the slab dip (Rontogianni et al., 2011) indicates an anomalous stress field that could be associated with the tip of a slab tear. Second, the proposed location of the tip of the slab tear (Spakman et al., 1988) is not located at the KTF. If tearing was an ongoing process that affected stress and strain in the slab, one would expect a southward migration of shallow deformation simultaneous with the tear propagation. The KTF has been active for the last 8 Myr, so it seems unlikely that shallow deformation has been affected by a southward propagation of a slab tear.

Even though our results cannot directly confirm or refute the hypothesis of a trench-parallel slab tear, a tear is not necessary to explain the observations within the seismically active part of the slab, especially the termination in seismicity across the KTF, which could be due to petrological changes instead.

7.3.2. Is There a Trench-Perpendicular Slab Tear?

A trench-perpendicular, vertical slab tear along the continuation of the KTF has previously been hypothesized based on the trench offset (Govers & Wortel, 2005; Royden & Papanikolaou, 2011; Suckale et al., 2009). Royden and Papanikolaou (2011) suggest that a slab tear is the cause of dextral strike-slip plate movement at the KTF. They attribute the differential plate movement to denser oceanic crust rolling back at a higher rate south of the KTF compared to lighter, more buoyant continental crust resisting rollback in the north. However, our tomographic models do not support a trench-perpendicular slab tear in the upper 100 km, an observation that is consistent with the conclusions of Pearce et al. (2012). Although our relocation study reveals a sharp termination of seismicity in the slab at the KTF, there is no noticeable offset marking a tear between the subducting crust just to the south and the north of the KTF (see the slab top model in Figure 11).

This observation is consistent across our tomographic models, the high-resolution images from 100 km north of the KTF (Pearce et al., 2012), and in the distribution of hypocenters contained in the subducting crusts.

7.3.3. Deformation of the Slab

Based on our observations, it appears that the deformation between subducting oceanic and continental crusts is widely distributed rather than occurring along a discrete fault. There are indeed a number of features in our models that point to a broad zone of deformation within the slab south of the KTF, instead of a vertical tear at the KTF.

First, there is a gradual offset in the position of the subducting crust and hypocenters south and north of the Gulf of Corinth (see slab top model in Figure 11), which implies that the center of deformation in the slab lies about 100 km south of the KTF.

Second, there is a v-shaped gap in deep seismicity below central Greece, which coincides approximately with that offset. Maximum hypocenter depth increases both toward the south and the north of this gap at 38.7°N (see red lines in Figure 11). This gap in seismicity might reflect a change in thermal conditions within the subducting crust due to the widely distributed deformation. One explanation would be that the subducting crust is stretched and thinned across the zone of deformation within the slab below the CHSZ, heating the crust more efficiently. Alternatively, seismicity terminates earlier due to warm mantle material flowing into the mantle wedge in this region, where the overriding crust is extending and thinning, also heating the subducting crust locally. A warmer subducting crust would reach the eclogite facies conditions earlier and thus prohibit the mechanisms enabling intermediate depth earthquakes or at least reduce their occurrence.

Taken together, these observations paint a picture of a slab that is deforming due to the subduction of crusts with different compositions. In contrast to earlier models (Pearce et al., 2012; Royden & Papanikolaou, 2011), the deformation of the slab occurs in a distributed fashion below the CHSZ rather than at the KTF, thus well within the oceanic part of the slab.

7.3.4. Stress Transfer to the Lower Overriding Crust

The location of the CHSZ and the zone of deformation within the slab correlate in their extents, which raises the question whether these two features are linked through coupling between the overriding and subducting crusts. This is especially relevant because the deformation taking place in the CHSZ is not well understood. The CHSZ is home to the largest strike-slip earthquake recorded on mainland Greece—the *M*6.4 Movri event of 2008 (fault plane marked in red in Figures 1 and 5; Gallovič et al., 2009). This earthquake, in which the lower overriding crust below the Movri mountains ruptured (Serpetsidaki et al., 2014), was unexpected

considering the absence of any comparable event in the historical record (Gallovič et al., 2009). According to Papadopoulos et al. (2010), the fault that ruptured had not been active for at least the last 300 years. The occurrence of a lower-crustal earthquake in the overriding plate, so close to the subduction interface, calls for a closer inspection of current plate-coupling models for the area. These models suggest little to no coupling along the whole interface (Baker et al., 1997; Jackson & McKenzie, 1988; Shaw & Jackson, 2010) or strong coupling limited to the upper 15 km of crust, with a shallow transition toward stable sliding between the ductile lower crust and the slab (Laigle et al., 2002). In the following section, we present evidence to help resolve the mismatch between a large earthquake rupturing the lower crust and the apparent lack of a transmittable force that could cause this earthquake.

There are a number of observations that support the suggestion that deformation in the CHSZ and within the slab is linked.

1. First, GPS data from McClusky et al. (2000) support the theory that the largest dextral shearing movement in the upper plate is realized within the CHSZ rather than at the KTF farther north. This suggests that while some differential plate motion offsets the trenches at Kephalonia, there is a larger force deforming the upper plate farther south.
2. Second, according to Serpetsidaki et al. (2014), the Movri earthquake is associated with an immature fault system with a predominantly dextral strike-slip movement, in line with the northern end of the CHSZ. This immaturity suggests that faulting started only recently, which matches our model of a slab in which deformation has been growing since the onset of differential subduction.
3. Third, although Serpetsidaki et al. (2014) place the Movri earthquake 50 km toward the backarc from the contact zone between overriding and subducting crusts in their model, our tomographic models suggest that the Movri event falls right into the area of thickened crust, where coupling between the crusts would be possible.

These observations all point toward at least some transfer of deformation between the overriding and subducting plates at the scale of the whole crust, and therefore, to a more complex situation occurring at the plate interface.

An updated understanding of the plate interface in the WHSZ is crucial to explain the occurrence of the Movri earthquake in the lower overriding crust. To explain the driving force behind the stress leading to the earthquake, two models have been proposed by Serpetsidaki et al. (2014). One model attributes strain to differential subduction rates, while the other model invokes the North Anatolian Fault as the driving force behind the strain. In the second model, they suggest that the premature fault system could be developing along a shear zone in the uppermost mantle which connects active crustal segments.

Based on the close spatial correlation between the zone of deformation in the slab, the northern part of the CHSZ and the Movri earthquake, we favor the differential slab rollback as the driving force behind stresses leading to the Movri earthquake. We also note that the westward propagation of the North Anatolian Fault into the northern part of the CHSZ might be focused by the deformation affecting both the slab and the CHSZ, possibly aided by the flow in the mantle wedge associated with differential subduction. Both models would not work if the lower crust was too ductile for stress transfer. In summary, our results are consistent with models that allow for partial coupling in the region, but more work is needed to determine the exact nature of this coupling.

8. Conclusions

We present new, high-resolution Vp and Vp/Vs ratio models and relocated hypocenters of the WHSZ. This new information helps us better understand the transition from oceanic subduction in the south of the region to continental subduction in the north, as well as the fate of slab-derived fluids. Our main results can be summarized in three points.

1. Intermediate depth seismicity occurs within a single plane throughout the southern part of the study area and is nearly nonexistent in the northern part, with an abrupt south-to-north transition occurring at the KTF. This change in seismicity appears to mark the boundary between two subducting domains: oceanic in the south and continental in the north and reflects their varying composition and fluid content. Slab dehydration seems to be particularly active in the southern part of the system, below the Peloponnesus,

where there is evidence for partial melting in the subarc mantle. Despite being nearly aseismic, the subducting continental crust in the north exhibits a low-velocity signature to at least 90 km depth (as imaged by *P* wave scattering potential $\delta\alpha/\alpha$). We interpret this low-velocity signature and seismic quiescence as reflecting an absence of fluids, which inhibits metamorphism and seismicity in a metastable continental subducting crust.

2. The transition between oceanic subduction with more rollback in the south to continental subduction with less rollback in the north is reflected by a smoothly deformed slab rather than a tear in the tomographic images. This slab deformation is accompanied by a gap in deep intraslab seismicity (>60 km depth), probably indicative of a change in thermal regime between south and north. The zone of slab deformation underlies the whole CHSZ and seems to affect the deformation in the overriding Aegean plate. We associate both the dextral strike-slip fault system of the 2008 Movri earthquake (*M*6.4) and the western extension of the North Anatolian Fault with this area of deformation, which is driven by differential subduction.
3. How fluids interact with the mantle wedge and the overriding crust seems to be impacted by the change in subduction style. Beneath the Hellenic arc, in the south, fluids emanating from the subducted oceanic crust appear to migrate directly upward into the mantle wedge, where they trigger partial melting. By contrast, in the central part of the WHSZ, our results suggest that slab-derived fluids might migrate toward the trench below an intact seal at the slab interface until they reach the lower crust of the overriding plate, where they precipitate silica.

Acknowledgments
We thank Maria Sachpazi, Jonny Wu, and the Associate Editor for their thoughtful reviews, which helped clarify and improve the original manuscript. The study was supported by funding from the Research Council of Norway for the project "Subduction zone Water and Metamorphism: A Modelling and Imaging Study" (project 231354). The services of E.J. Farmer Editing and Proofreading were used. Earthquake catalogs and phase arrival data were downloaded from the International Seismological Centre http://www.isc.ac.uk/ and the National Observatory of Athens http://bbnet.gein.noa.gr/HL/. Seismic waveform data from the MEDUSA network and selected stations of the Hellenic Unified Seismic Network are archived at the Incorporated Research Institutions for Seismology (IRIS) Data Management Center (DMC) (http://ds.iris.edu/ds/nodes/dmc) under temporary network code XS (2006–2009) and permanent network code HL, respectively. Waveform data of the EGELADOS stations can be downloaded from the Observatories and Research Facilities for European Seismology (ORFEUS) European Integrated Data Archive (EIDA) (http://www.orfeus-eu.org/data/eida/) under temporary network code Z3 (2005–2007). Shuttle Radar Topography Mission (SRTM) topography data for Figures 1 and 5 were downloaded from the U.S. Geological Survey at https://dds.cr.usgs.gov/srtm/. Bathymetry data in these figures are from the Smith and Sandwell bathymetry database at the Scripps Institution of Oceanography, University of California at San Diego, at http://topex.ucsd.edu/marine_topo/. Maps were created with the m_map Matlab toolbox (https://www.eoas.ubc.ca/~rich/map.html. A catalog of the relocated earthquakes, the tomographic models of *P* velocity and Vp/Vs ratio, the slab top model, and coastlines of Greece (from Wessel & Smith, 1996) are included in the supporting information of this paper. These supporting information are available online and contain a description about how the data sets can be readily displayed in Paraview (Ahrens et al., 2005).

References

Abers, G. A., van Keken, P. E., & Hacker, B. R. (2017). The cold and relatively dry nature of mantle forearcs in subduction zones. *Nature Geoscience*, *10*, 333–337. https://doi.org/10.1038/ngeo2922

Ahrens, J., Geveci, B., & Law, C. (2005). ParaView: An end-user tool for large-data visualization. *Visualization Handbook*, *836*, 717–731. https://doi.org/10.1016/B978-012387582-2/50038-1

Amante, C., & Eakins, B. W. (2009). *ETOPO1 1 arc-minute global relief model: Procedures, data sources and analysis*. Boulder, CO: NOAA Technical Memorandum NESDIS NGDC-24. National Geophysical Data Center

Audet, P., & Bürgmann, R. (2014). Possible control of subduction zone slow-earthquake periodicity by silica enrichment. *Nature*, *510*, 389–392. https://doi.org/10.1038/nature13391

Austrheim, H. (1987). Eclogitization of lower crustal granulites by fluid migration through shear zones. *Earth and Planetary Science Letters*, *81*, 221–232.

Baker, C., Hatzfeld, D., Lyon-Caen, H., Papadimitriou, E., & Rigo, A. (1997). Earthquake mechanisms of the Adriatic Sea and Western Greece: Implications for the oceanic subduction-continental collision transition. *Geophysical Journal International*, *131*(3), 559–594. https://doi.org/10.1111/j.1365-246x.1997.tb06600.x

Benetatos, C., Kiratzi, a., Papazachos, C., & Karakaisis, G. (2004). Focal mechanisms of shallow and intermediate depth earthquakes along the Hellenic Arc. *Journal of Geodynamics*, *37*(2), 253–296. https://doi.org/10.1016/j.jog.2004.02.002

Bijwaard, H., Spakman, W., & Engdahl, E. R. (1998). Closing the gap between regional and global travel time tomography. *Journal of Geophysical Research*, *103*(B12), 30,055–30,078. https://doi.org/10.1029/98JB02467

Bleibinhaus, F. (2003). 3D simultaneous refraction and reflection seismic travel time tomography and application to deep seismic TRANSALP wide-angle data (Doctoral dissertation). München: Ludwig-Maximilians-Universitat Munchen. Retrieved from https://edoc.ub.uni-muenchen.de/1263/

Bohnhoff, M., Makris, J., Papanikolaou, D., & Stavrakakis, G. (2001). Crustal investigations of the Hellenic subduction zone using wide aperture seismic data. *Tectonophysics*, *343*, 239–262.

Bostock, M. G., Hyndman, R. D., Rondenay, S., & Peacock, S. M. (2002). An inverted continental Moho and serpentinization of the forearc mantle. *Nature*, *417*(6888), 536–538. https://doi.org/10.1038/417536a

Breeding, C. M., & Ague, J. J. (2002). Slab-derived fluids and quartz-vein formation in an accretionary prism, Otago Schist, New Zealand. *Geology*, *30*(6), 499–502. https://doi.org/10.1130/0091-7613(2002)030<0499:SDFAQV>2.0.CO;2

Brudzinski, M. R., Thurber, C. H., Hacker, B. R., & Engdahl, E. R. (2007). Global prevalence of double Benioff zones. *Science*, *316*(5830), 1472–1474. https://doi.org/10.1126/science.1139204

Brüstle, A. (2012). Seismicity of the eastern Hellenic subduction zone (Doctoral dissertation). Ruhr-Universität Bochum, Bochum, Germany. Retrieved from https://www-brs.ub.ruhr-uni-bochum.de/netahtml/HSS/Diss/BruestleAndrea/diss.pdf

Clift, P., & Vannucchi, P. (2004). Controls on tectonic accretion versus erosion in subduction zones: Implications for the origin and recycling of the continental crust. *Reviews of Geophysics*, *42*, RG2001. https://doi.org/10.1029/2003RG000127

Davey, F. J., & Ristau, J. (2011). Fore-arc mantle wedge seismicity under northeast New Zealand. *Tectonophysics*, *509*(3-4), 272–279. https://doi.org/10.1016/j.tecto.2011.06.017

Del Ben, A., Mocnik, A., Volpi, V., & Karvelis, P. (2015). Old domains in the South Adria plate and their relationship with the West Hellenic front. *Journal of Geodynamics*, *89*, 15–28. https://doi.org/10.1016/j.jog.2015.06.003

Diehl, T., Kissling, E., & Bormann, P. (2002). Tutorial for consistent phase picking at local to regional distances. In P. Bormann (Ed.), *New manual of seismological observatory practice (NMSOP-2)* (chap. IS 11.4, pp. 1–21). Potsdam: IASPEI, GFZ German Research Centre for Geosciences. https://doi.org/10.2312/GFZ.NMSOP-2_ IS_11.4

Durand, V., Bouchon, M., Floyd, M. A., Theodulidis, N., Marsan, D., Karabulut, H., & Schmittbuhl, J. (2014). Observation of the spread of slow deformation in Greece following the breakup of the slab. *Geophysical Research Letters*, *41*, 7129–7134. https://doi.org/10.1002/2014GL061408

Eberhart-Phillips, D. (1990). Three-dimensional *P* and *S* velocity structure in the Coalinga region, California. *Journal of Geophysical Research*, *95*(B10), 15,343–15,363. https://doi.org/10.1029/JB095iB10p15343

Eberhart-Phillips, D., & Bannister, S. (2010). 3-D imaging of Marlborough, New Zealand, subducted plate and strike-slip fault systems. *Geophysical Journal International*, *182*(1), 73–96. https://doi.org/10.1111/j.1365-246x.2010. 04621.x

Evans, J. R., Eberhart-Phillips, D., & Thurber, C. H. (1999). User's manual for SIMULPS12 for imaging Vp and Vp/Vs: A derivative of the "Thurber" tomographic inversion SIMUL3 for local earthquakes and explosions. *U.S. Geological Survey Open File Report*, 94–431.

Finetti, I. R., & Del Ben, A. (2005). Crustal tectono-stratigraphic setting of the adriatic sea from new CROP seismic data. In I. R. Finelli (Ed.), *Deep Seismic Exploration of the Central Mediterranean and Italy* (chap. 23). Amsterdam: Elsevier.

Flerit, F., Armijo, R., King, G., & Meyer, B. (2004). The mechanical interaction between the propagating North Anatolian Fault and the back-arc extension in the Aegean. *Earth and Planetary Science Letters*, *224*(3-4), 347–362. https://doi.org/10.1016/j.epsl.2004.05.028

Galanis, O., Papazachos, C., Scordilis, E., & Hatzidimitriou, P. (2006). Improved earthquake locations in Greece using the DD algorithm and a 3D velocity model. In *First European Conference on Earthquake Engineering and Seismology* (810 pp.). Geneva, Switzerland.

Gallovič, F., Zahradník, J., Křížová, D., Plicka, V., Sokos, E., Serpetsidaki, A., & Tselentis, G. A. (2009). From earthquake centroid to spatial-temporal rupture evolution: Mw 6.3 Movri Mountain earthquake, June 8, 2008, Greece. *Geophysical Research Letters*, *36*, L21310. https://doi.org/10.1029/2009GL040283

Gesret, A., Laigle, M., Diaz, J., Sachpazi, M., Charalampakis, M., & Hirn, A. (2011). Slab top dips resolved by teleseismic converted waves in the Hellenic subduction zone. *Geophysical Research Letters*, *38*, L20304. https://doi.org/10.1029/2011GL048996

Govers, R., & Wortel, M. J. R. (2005). Lithosphere tearing at STEP faults: Response to edges of subduction zones. *Earth and Planetary Science Letters*, *236*(1-2), 505–523. https://doi.org/10.1016/j.epsl.2005.03.022

Haslinger, F., & Kissling, E. (2001). Investigating effects of 3-D ray tracing methods in local earthquake tomography. *Physics of the Earth and Planetary Interiors*, *123*(2-4), 103–114. https://doi.org/10.1016/S0031-9201(00) 00204-1

Haslinger, F., Kissling, E., Ansorge, J., Hatzfeld, D., Papadimitriou, E. E., Karakostas, V., et al. (1999). 3D Crustal structure from local earthquake tomography around Gulf of Arta. *Tectonophysics*, *304*, 210–218.

Hatzfeld, D. (1994). On the shape of the subducting slab beneath the Peloponnese, Greece. *Geophysical Research Letters*, *21*(3), 173–176. https://doi.org/10.1029/93GL03079

Hatzfeld, D., & Martin, C. (1992). Intermediate depth seismicity in the Aegean defined by teleseismic data. *Earth and Planetary Science Letters*, *113*(1-2), 267–275. https://doi.org/10.1016/0012-821X(92)90224-J

Havskov, J., & Ottemöller, L. (1999). SeisAn earthquake analysis software. *Seismological Research Letters*, *70*(5), 532–534.

Hyndman, R. D., McCrory, P. A., Wech, A., Kao, H., & Ague, J. (2015). Cascadia subducting plate fluids channelled to fore-arc mantle corner: ETS and silica deposition. *Journal of Geophysical Research: Solid Earth*, *120*, 4344–4358. https://doi.org/10.1002/2015JB011920

International Seismological Centre (2017). *On-line bulletin*. Thatcham, UK: International Seismological Centre. Retrieved from http://www.isc.ac.uk

Jackson, J., & McKenzie, D. (1988). The relationship between plate motions and seismic moment tensors, and the rates of active deformation in the Mediterranean and Middle East. *Geophysical Journal International*, *93*(1), 45–73. https://doi.org/10.1111/j.1365-246x.1988.tb01387.x

Karakonstantis, A., & Papadimitriou, P. (2010). Earthquake relocation in Greece using a unified and homogenized seismological catalogue. *Bulletin of the Geological Society of Greece*, *43*(4), 2043–2052.

Karastathis, V. K., Mouzakiotis, E., Ganas, A., & Papadopoulos, G. A. (2015). High-precision relocation of seismic sequences above a dipping Moho: The case of the January–February 2014 seismic sequence on Cephalonia island (Greece). *Solid Earth*, *6*, 173–184. https://doi.org/10.5194/se-6-173-2015

Kennett, B. L. N., Engdahl, E. R., & Buland, R. (1995). Constraints on seismic velocities in the Earth from traveltimes. *Geophysical Journal International*, *122*, 108–124. https://doi.org/10.1111/j.1365-246x.1995. tb03540.x

Kissling, E., Ellsworth, W. L., Eberhart-Phillips, D., & Kradolfer, U. (1994). Initial reference models in local earthquake tomography. *Journal of Geophysical Research*, *99*(B10), 19,635–19,646.

Klein, F. W. (2002). *User's guide to HYPOINVERSE-2000, a FORTRAN program to solve for earthquake locations and magnitudes*. Menlo Park CA: U.S. Geological Survey Open File Report 02-171.

Klemd, R., John, T., Scherer, E. E., Rondenay, S., & Gao, J. (2011). Changes in dip of subducted slabs at depth: Petrological and geochronological evidence from HP-UHP rocks (Tianshan, NW-China). *Earth and Planetary Science Letters*, *310*(1-2), 9–20. https://doi.org/10.1016/j.epsl.2011.07.022

Kokinou, E., Kamberis, E., Vafidis, A., Monopolis, D., Ananiadis, G., & Zelilidis, A. (2005). Deep seismic reflection data from offshore Western Greece: A new crustal model for the Ionian Sea. *Journal of Petroleum Geology*, *28*(2), 185–202. https://doi.org/10.1111/j.1747-5457.2005.tb00079.x

Kokinou, E., Papadimitriou, E., Karakostas, V., Kamberis, E., & Vallianatos, F. (2006). The Kefalonia Transform Zone (offshore Western Greece) with special emphasis to its prolongation towards the Ionian Abyssal Plain. *Marine Geophysical Researches*, *27*(4), 241–252. https://doi.org/10.1007/s11001-006-9005-2

Konstantinou, K. I., Melis, N. S., & Boukouras, K. (2010). Routine regional moment tensor inversion for earthquakes in the Greek region: The National Observatory of Athens (NOA) database (2001–2006). *Seismological Research Letters*, *81*(5), 750–760. https://doi.org/10.1785/gssrl

Koulakov, I., Kaban, M. K., Tesauro, M., & Cloetingh, S. (2009). P- and S-velocity anomalies in the upper mantle beneath Europe from tomographic inversion of ISC data. *Geophysical Journal International*, *179*(1), 345–366. https://doi.org/10.1111/j.1365-246x.2009.04279.x

Laigle, M., Hirn, A., Sachpazi, M., & Clément, C. (2002). Seismic coupling and structure of the Hellenic subduction zone in the Ionian Islands region. *Earth and Planetary Science Letters*, *200*(3-4), 243–253. https://doi.org/10.1016/S0012-821X(02)00654-4

Lamara, S. (2015). 3D waveform tomography of the Hellenic subduction zone (Doctoral dissertation). Bochum, Germany: Ruhr-Universitat Bochum. Retrieved from http://hss-opus.ub.ruhr-uni-bochum.de/opus4/files/4415/diss.pdf

Li, X., Bock, G., Vafidis, A., Kind, R., Harjes, H. P., Hanka, W., et al. (2003). Receiver function study of the Hellenic subduction zone: Imaging crustal thickness variations and the oceanic Moho of the descending African lithosphere. *Geophysical Journal International*, *155*(2), 733–748. https://doi.org/10.1046/j.1365-246x.2003.02100.x

Lienert, B. R., & Havskov, J. (1995). A computer program for locating earthquakes both locally and globally. *Seismological Research Letters*, *66*(5), 26–36. https://doi.org/10.1785/gssrl.66.5.26

MacKenzie, L. S., Abers, G. A., Rondenay, S., & Fischer, K. M. (2010). Imaging a steeply dipping subducting slab in Southern Central America. *Earth and Planetary Science Letters*, *296*(3-4), 459–468. https://doi.org/10.1016/j.epsl.2010.05.033

Manning, C. E. (1994). The solubility of quartz in H_2O in the lower crust and upper mantle. *Geochimica et Cosmochimica Acta*, *58*(22), 4831–4839.

McClusky, S., Balassanian, S., Barka, A., Demir, C., Ergintav, S., Georgiev, I., et al. (2000). Global Positioning System constraints on plate kinematics and dynamics in the eastern Mediterranean and Caucasus. *Journal of Geophysical Research*, *105*(B3), 5695–5719. https://doi.org/10.1029/1999JB900351

McKenzie, D. (1972). Active tectonics of the Mediterranean region. *Geophysical Journal International*, *30*, 109–185.

Meighan, H. E., Ten Brink, U., & Pulliam, J. (2013). Slab tears and intermediate-depth seismicity. *Geophysical Research Letters*, *40*, 4244–4248. https://doi.org/10.1002/grl.50830

Nakajima, J., Uchida, N., Shiina, T., Hasegawa, A., Hacker, B. R., & Kirby, S. H. (2013). Intermediate-depth earthquakes facilitated by eclogitization-related stresses. *Geology*, *41*(6), 659–662. https://doi.org/10.1130/G33796.1

Nixon, C. W., McNeill, L. C., Bull, J. M., Bell, R. E., Gawthorpe, R. L., Henstock, T. J., et al. (2016). Rapid spatiotemporal variations in rift structure during development of the Corinth Rift, central Greece. *Tectonics*, *35*, 1225–1248. https://doi.org/10.1002/2015TC004026

Olive, J. A., Pearce, F., Rondenay, S., & Behn, M. D. (2014). Pronounced zonation of seismic anisotropy in the Western Hellenic subduction zone and its geodynamic significance. *Earth and Planetary Science Letters*, *391*, 100–109. https://doi.org/10.1016/j.epsl.2014.01.029

Papadopoulos, G. A., Karastathis, V., Kontoes, C., Charalampakis, M., Fokaefs, A., & Papoutsis, I. (2010). Crustal deformation associated with east Mediterranean strike-slip earthquakes: The 8 June 2008 Movri (NW Peloponnese), Greece, earthquake (Mw6.4). *Tectonophysics*, *492*(1-4), 201–212. https://doi.org/10.1016/j.tecto.2010.06.012

Papanikolaou, D. J., & Royden, L. H. (2007). Disruption of the Hellenic arc: Late Miocene extensional detachment faults and steep Pliocene-Quaternary normal faults—Or what happened at Corinth? *Tectonics*, *26*, TC5003. https://doi.org/10.1029/2006TC002007

Papazachos, B. C., Karakostas, V. G., Papazachos, C. B., & Scordilis, E. M. (2000). The geometry of the Wadati-Benioff zone and lithospheric kinematics in the Hellenic arc. *Tectonophysics*, *319*(4), 275–300. https://doi.org/10.1016/S0040-1951(99)00299-1

Papazachos, C., & Nolet, G. (1997). *P* and *S* deep velocity structure of the Hellenic area obtained by robust nonlinear inversion of travel times. *Journal of Geophysical Research*, *102*, 8349–8367. https://doi.org/10.1029/96JB03730

Pe-Piper, G., & Piper, D. J. W. (2007). Neogene backarc volcanism of the Aegean: New insights into the relationship between magmatism and tectonics. *Geological Society of America Special Papers*, *418*(02), 17–31. https://doi.org/10.1130/2007.2418(02)

Peacock, S. M. (1993). The importance of blueschist -> eclogite dehydration reactions in subducting oceanic crust. *Geological Society of America Bulletin*, *105*(5), 684–694. https://doi.org/10.1130/0016-7606(1993)105<0684:TIOBED>2.3.CO;2

Pearce, F. D., Rondenay, S., Sachpazi, M., Charalampakis, M., & Royden, L. H. (2012). Seismic investigation of the transition from continental to oceanic subduction along the western Hellenic subduction Zone. *Journal of Geophysical Research*, *117*, B07306. https://doi.org/10.1029/2011JB009023

Piromallo, C. (2003). *P* wave tomography of the mantle under the Alpine-Mediterranean area. *Journal of Geophysical Research*, *108*(B2), 2065. https://doi.org/10.1029/2002JB001757

Ramachandran, K., & Hyndman, R. D. (2012). The fate of fluids released from subducting slab in northern Cascadia. *Solid Earth*, *3*(1), 121–129. https://doi.org/10.5194/se-3-121-2012

Reilinger, R., McClusky, S., Vernant, P., Lawrence, S., Ergintav, S., Cakmak, R., et al. (2006). GPS constraints on continental deformation in the Africa-Arabia-Eurasia continental collision zone and implications for the dynamics of plate interactions. *Journal of Geophysical Research*, *111*, B05411. https://doi.org/10.1029/2005JB004051

Reyners, M., Eberhart-Phillips, D., Stuart, G., & Nishimura, Y. (2006). Imaging subduction from the trench to 300 km depth beneath the central North Island, New Zealand, with Vp and Vp/Vs. *Geophysical Journal International*, *165*(2), 565–583. https://doi.org/10.1111/j.1365-246x.2006.02897.x

Rizzo, A. L., Caracausi, A., Chavagnac, V., Nomikou, P., Polymenakou, P. N., Mandalakis, M., et al. (2016). Kolumbo submarine volcano (Greece): An active window into the Aegean subduction system. *Scientific Reports*, *6*(February), 28013. https://doi.org/10.1038/srep28013

Rontogianni, S., Konstantinou, N. S., Melis, C. P., & Evangelidis (2011). Slab stress field in the Hellenic subduction zone as inferred from intermediate-depth earthquakes. *Earth, Planets and Space*, *63*(2), 139–144. https://doi.org/10.5047/eps.2010.11.011

Royden, L. H., & Papanikolaou, D. J. (2011). Slab segmentation and late Cenozoic disruption of the Hellenic arc. *Geochemistry, Geophysics, Geosystems*, *12*, Q03010. https://doi.org/10.1029/2010GC003280

Sachpazi, M., Hirn, A., Clément, C., Haslinger, F., Laigle, M., Kissling, E., et al. (2000). Western Hellenic subduction and Cephalonia transform: Local earthquakes and plate transport and strain. *Tectonophysics*, *319*(4), 301–319. https://doi.org/10.1016/S0040-1951(99)00300-5

Sachpazi, M., Laigle, M., Charalampakis, M., Diaz, J., Kissling, E., Gesret, A., et al. (2016). Segmented Hellenic slab rollback driving Aegean deformation and seismicity. *Geophysical Research Letters*, *43*, 651–658. https://doi.org/10.1002/2015GL066818

Serpetsidaki, A., Elias, P., Ilieva, M., Bernard, P., Briole, P., Deschamps, A., et al. (2014). New constraints from seismology and geodesy on the Mw = 6.4 2008 Movri (Greece) earthquake: Evidence for a growing strike-slip fault system. *Geophysical Journal International*, *198*(3), 1373–1386. https://doi.org/10.1093/gji/ggu212

Serpetsidaki, A., Sokos, E., & Tselentis, G.-A. (2016). A ten year moment tensor database for western Greece. *Physics and Chemistry of the Earth, Parts A/B/C*, *95*, 2–9. https://doi.org/10.1016/j.pce.2016.04.007

Shaw, B., & Jackson, J. (2010). Earthquake mechanisms and active tectonics of the Hellenic subduction zone. *Geophysical Journal International*, *181*(2), 966–984. https://doi.org/10.1111/j.1365-246x.2010.04551.x

Sodoudi, F., Brüstle, A., Meier, T., Kind, R., Friederich, W., & Egelados Working Group (2015). Receiver function images of the Hellenic subduction zone and comparison to microseismicity. *Solid Earth*, *6*(1), 135–151. https://doi.org/10.5194/se-6-135-2015

Spakman, W., Wortel, M. J. R., & Vlaar, N. J. (1988). The Hellenic subduction zone: A tomographic image and its geodynamic implications. *Geophysical Research Letters*, *15*(1), 60–63. https://doi.org/10.1029/GL015i001p00060

Speranza, F., Minelli, L., Pignatelli, A., & Chiappini, M. (2012). The Ionian Sea: The oldest in situ ocean fragment of the world? *Journal of Geophysical Research*, *117*, B12101. https://doi.org/10.1029/2012JB009475

Suckale, J., Rondenay, S., Sachpazi, M., Charalampakis, M., Hosa, A., & Royden, L. H. (2009). High-resolution seismic imaging of the western Hellenic subduction zone using teleseismic scattered waves. *Geophysical Journal International*, *178*(2), 775–791. https://doi.org/10.1111/j.1365-246x.2009.04170.x

Syracuse, E. M., van Keken, P. E., Abers, G. A., Suetsugu, D., Bina, C., Inoue, T., et al. (2010). The global range of subduction zone thermal models. *Physics of the Earth and Planetary Interiors*, *183*, 73–90. https://doi.org/10.1016/j.pepi.2010.02.004

Theunissen, T., Chevrot, S., Sylvander, M., Monteiller, V., Calvet, M., Villaseñor, M., et al. (2018). Absolute earthquake locations using 3-D versus 1-D velocity models below a local seismic network: Example from the Pyrenees. *Geophysical Journal International*, *212*, 1806–1828. https://doi.org/10.1093/gji/ggx472

Thurber, C. H. (1983). Earthquake locations and three-dimensional crustal structure in the Coyote Lake Area, central California. *Journal of Geophysical Research*, *88*(B10), 8226–8236. https://doi.org/10.1029/JB088iB10p08226

Thurber, C. H., & Eberhart-Phillips, D. (1999). Local earthquake tomography with flexible gridding. *Computers and Geosciences*, *25*(7), 809–818. https://doi.org/10.1016/S0098-3004(99)00007-2

Uchida, N., Kirby, S. H., Okada, T., Hino, R., & Hasegawa, A. (2010). Supraslab earthquake clusters above the subduction plate boundary offshore Sanriku, northeastern Japan: Seismogenesis in a graveyard of detached seamounts? *Journal of Geophysical Research*, *115*, B09308. https://doi.org/10.1029/2009JB006797

Um, J., & Thurber, C. H. (1987). A fast algorithm for two-point ray tracing. *Bulletin of the Seismological Society of America*, *77*(June), 972–986.

Unsworth, M., & Rondenay, S. (2013). Mapping the distribution of fluids in the crust and lithospheric mantle utilizing geophysical methods. In M. Unsworth & S. Rondenay (Eds.), *Metasomatism and the chemical transformation of rock, lecture notes in Earth System Sciences* (pp. 535–598). Berlin: Springer-Verlag. https://doi.org/10.1007/978-3-642-28394-9_13

van Keken, P. E., Kita, S., & Nakajima, J. (2012). Thermal structure and intermediate-depth seismicity in the Tohoku-Hokkaido subduction zones. *Solid Earth*, *3*(2), 355–364. https://doi.org/10.5194/se-3-355-2012

Vassilakis, E., Royden, L. H., & Papanikolaou, D. (2011). Kinematic links between subduction along the Hellenic trench and extension in the Gulf of Corinth, Greece: A multidisciplinary analysis. *Earth and Planetary Science Letters*, *303*(1-2), 108–120. https://doi.org/10.1016/j.epsl.2010.12.054

von Huene, R., Reston, T., Kukowski, N., Dehghani, G., & Weinrebe, W. (1997). A subducting seamount beneath the Mediterranean Ridge. *Tectonophysics*, *271*(3-4), 249–261. https://doi.org/10.1016/S0040-1951(96) 00241-7

Waldhauser, F. (2012). *User guide to HypoDD version 2.1b*. Palisades, New York: Lamont-Doherty Earth Observatory.

Waldhauser, F., & Ellsworth, W. L. (2000). A double-difference earthquake location algorithm: Method and application to the northern Hayward fault, California. *Bulletin of the Seismological Society of America*, *6*, 1353–1368.

Wessel, P., & Smith, W. H. F. (1996). A global, self-consistent, hierarchical, high-resolution shoreline. *Journal of Geophysical Research*, *101*(B4), 8741–8743.

Wortel, M. J. R., & Spakman, W. (2000). Subduction and slab detachment in the Mediterranean-Carpathian region. *Science*, *290*(5498), 1910–1917. https://doi.org/10.1126/science.290.5498.1910

Zelt, B. C., Taylor, B., Sachpazi, M., & Hirn, A. (2005). Crustal velocity and Moho structure beneath the Gulf of Corinth, Greece. *Geophysical Journal International*, *162*(1), 257–268. https://doi.org/10.1111/j.1365-246x. 2005.02640.x

Zhang, H., Thurber, C. H., Shelly, D., Ide, S., Beroza, G. C., & Hasegawa, A. (2004). High-resolution subducting-slab structure beneath northern Honshu, Japan, revealed by double-difference tomography. *Geology*, *32*(4), 361–364. https://doi.org/10.1130/G20261.2

Zhu, H., Bozdăg, E., & Tromp, J. (2015). Seismic structure of the European upper mantle based on adjoint tomography. *Geophysical Journal International*, *201*(1), 18–52. https://doi.org/10.1093/gji/ggu492